



LAWRENCE  
LIVERMORE  
NATIONAL  
LABORATORY

# Constraints on fallout melt glass formation from a near-surface nuclear test

G. R. Eppich, K. B. Knight, T. W. Jacomb-Hood,  
G. D. Spriggs, I. D. Hutcheon

February 24, 2014

Journal of Radioanalytical and Nuclear Chemistry

## **Disclaimer**

---

This document was prepared as an account of work sponsored by an agency of the United States government. Neither the United States government nor Lawrence Livermore National Security, LLC, nor any of their employees makes any warranty, expressed or implied, or assumes any legal liability or responsibility for the accuracy, completeness, or usefulness of any information, apparatus, product, or process disclosed, or represents that its use would not infringe privately owned rights. Reference herein to any specific commercial product, process, or service by trade name, trademark, manufacturer, or otherwise does not necessarily constitute or imply its endorsement, recommendation, or favoring by the United States government or Lawrence Livermore National Security, LLC. The views and opinions of authors expressed herein do not necessarily state or reflect those of the United States government or Lawrence Livermore National Security, LLC, and shall not be used for advertising or product endorsement purposes.

**1 Constraints on fallout melt glass formation from a near-surface nuclear test****2 Gary R. Eppich; Kim B. Knight; Timothy W. Jacomb-Hood; Gregory D. Spriggs; Ian D. Hutcheon****6 Abstract**

7 The formation of fallout glass in near-surface nuclear tests occurs when melted environmental  
8 materials (surficial rocks and sediment) are swept up into the fireball and incorporate bomb debris  
9 before solidifying. Formation mechanisms of fallout are poorly constrained, yet if understood, can  
10 provide insight into the physical and chemical conditions of the fireball. Here we present major  
11 element and actinide composition data from a population of 28 aerodynamically-shaped pieces of  
12 fallout glass produced from a single near-surface nuclear detonation, and use these data to  
13 reconstruct the chemical changes that occurred in these melts prior to solidification. Glass major  
14 element compositions are similar to the compositions of six bulk surface sediments collected  
15 proximal to test ground zero, indicating that composition of local geology is a primary control on  
16 bulk fallout chemical composition. These sediment-derived melts were not held at temperatures  
17 above their boiling points long enough for significant major element volatilization to occur, with the  
18 possible exception of sodium, the most volatile major element. Fallout glass enrichment in U  
19 concentration (14.73 to 32.85  $\mu\text{g/g}$ ) and  $^{235}\text{U}/^{238}\text{U}$  (2.321 to 7.725) relative to bulk sediments (U =  
20  $\sim 4.6 \mu\text{g/g}$ ,  $^{235}\text{U}/^{238}\text{U} = 0.00725$ ) indicates that vaporized, residual fuel was incorporated into the  
21 melts prior to solidification, likely within seconds. Variation observed in fallout glass uranium  
22 isotopic composition is consistent with two-component mixing, with naturally-occurring uranium  
23 and residual uranium fuel as the two end-members. Fallout glass  $^{234}\text{U}/^{235}\text{U}$  and  $^{236}\text{U}/^{235}\text{U}$  ratios fall  
24 within a restricted range of 0.01078 to 0.01093 and 0.00484 to 0.00500, respectively, and appear to  
25 be characteristic of fallout produced by this nuclear test. Model ages of the residual fuel in fallout,  
26 calculated using the  $^{234}\text{U}$ - $^{230}\text{Th}$  and  $^{235}\text{U}$ - $^{231}\text{Pa}$  chronometers, are tens to hundreds of years older than  
27 the known ages of nuclear weapon production. These model ages are systematically inaccurate,  
28 biased towards older ages, and are consistent with two-component mixing between naturally-  
29 occurring  $^{230}\text{Th}$  and  $^{231}\text{Pa}$  in local sediment and decay-derived  $^{230}\text{Th}$  and  $^{231}\text{Pa}$  from residual nuclear  
30 fuel. Fallout glass  $^{230}\text{Th}/^{232}\text{Th}$  ratios, when corrected for ingrowth of  $^{230}\text{Th}$  from the decay of  $^{234}\text{U}$ , fall

31 within the range observed in local sediment, yet remain heterogeneous, suggesting that naturally-  
32 occurring isotopic heterogeneity is preserved in fallout. Multiple processes such as mixing,  
33 agglomeration of melted sediment-derived droplets, and incorporation of condensates must all occur  
34 within the timescale between sediment melting and melt solidification.

35

36

### 37 **Introduction**

38 Glassy fallout, a byproduct of near surface nuclear detonations, may be one of the primary materials  
39 available for investigation following a nuclear event. During the era of near-surface nuclear testing in  
40 the United States (1945-1973), fallout was produced from a multitude of tests and originally studied  
41 as a radiation hazard. The legacy of near-surface testing persists to this day, primarily in the form of  
42 radioactive glassy debris. Macro-scale fallout glass forms when environmental materials are swept  
43 up into the fireball and partially or fully melted, interacting with debris from the device prior to  
44 cooling of the fireball below the condensation temperature of most relevant chemical species  
45 (Glasstone and Dolan, 1977). Although there is some variation with respect to yield, the time window  
46 for such interactions and cooling is of order seconds (Glasstone and Dolan, 1977, Cassata *et al.*, in  
47 review).

48

49 Radioactive glasses formed by the Trinity test, collectively termed *trinitite*, have been extensively  
50 studied (*e.g.*, Adams *et al.*, 1960; Hermes and Strickfaden, 2005; Parekh *et al.*, 2006, Eby *et al.*, 2010;  
51 Fahey *et al.*, 2010; Belloni *et al.*, 2011; Bellucci *et al.*, 2012; Bellucci and Simonetti, 2012; Bellucci *et*  
52 *al.*, 2013a, b). The silicate melt glasses produced in the Trinity event have been shown to contain  
53 fission products, activation products, residual nuclear fuel, and enrichments in elements derived  
54 from non-nuclear device components. Trinitite is interpreted to have formed *in-situ*, at the site of  
55 fireball-sediment interaction, although some studies (Hermes and Strickfaden, 2005; Belloni *et al.*,  
56 2011) suggest that the upper layer of trinitite glass contains partially-mixed remnants of a “silicate  
57 melt rain”, some of which was deposited on the ground while molten, and fused with molten *in situ*  
58 trinitite before either component solidified. Belloni *et al.* (2011) provide evidence that the fused

59 “silicate melt rain” component of trinitite is more radioactive than the fraction of the glass formed *in-*  
60 *situ*, indicating that this component of silicate melt interacted with the fireball to a greater degree  
61 than those melts formed on the surface. Eby *et al.* (2010) reported the existence of aerodynamic  
62 fallout glasses from the Trinity event – often with spherical or oblong morphologies. These types of  
63 glasses have not yet been the focus of significant chemical study, but also clearly illustrate that glassy  
64 fallout may form through several different mechanisms, even in the same event.

65

66 In this study, we seek to better constrain formation mechanisms for macro-scale glassy fallout  
67 production. We analyzed twenty-eight quasi-spherical to irregularly-shaped pieces of fallout glasses  
68 produced from a single near-surface nuclear test. The samples all exhibit aerodynamic morphologies,  
69 or are a conglomeration of aerodynamic shapes, suggesting they were molten and quenched prior to  
70 deposition on the surface. These samples may be analogous to the “spheroids” studied by Hermes  
71 and Strickfaden (2005) and Eby *et al.* (2010), and the “silicate melt rain” hypothesized by Belloni *et*  
72 *al.* (2011). In order to characterize the initial chemical composition of the melts, we sampled  
73 nominally uncontaminated sediment (i.e., sediment devoid of local fallout contributions) from the  
74 vicinity of the test. The goals of this study are twofold: 1) to characterize chemical and isotopic  
75 compositional heterogeneity across a range of morphologies of single pieces of fallout glass produced  
76 in a near-surface nuclear test, and 2) to place constraints on the chemical and isotopic evolution of  
77 fallout to explain the compositional data. We also use the  $^{234}\text{U}$ - $^{230}\text{Th}$  and  $^{235}\text{U}$ - $^{231}\text{Pa}$  chronometers,  
78 recently applied to the age-dating of nuclear fuel (LaMont and Hall, 2005; Varga and Surányi, 2007;  
79 Williams and Gaffney, 2011; Eppich *et al.*, 2013), to explore if these data can be used to constrain the  
80 production age of fallout produced by a uranium-fueled nuclear device.

81

## 82 **Samples and Methods**

### 83 *Sample collection, selection, and initial characterization*

84 Six samples were collected from the upper 10 cm of exposed sediment, tens to hundreds of meters  
85 from the site of the detonation (hereafter referred to as “ground zero”). Three sediment samples  
86 were collected 0.12 to 0.9 km from ground zero, away from the activity plume, to most accurately

87 characterize the chemical composition of the pre-detonation environment. A second set of sediment  
88 samples was collected from a greater distance (~2-3 km from ground zero), and captures some of the  
89 local compositional variation. Sediment samples were collected dry, and contained little to no organic  
90 matter. Sediment grain size varies from fine-grained sand to small pebbles, but was not characterized  
91 in detail for this study. After collection, sediments were inspected to ensure the exclusion of macro-  
92 scale glassy fallout material. The potential for contamination of sediment by micro-scale fallout from  
93 the nuclear event is addressed below.

94

95 Fallout glass samples were collected along the path of the fallout plume, within ~600 m from ground  
96 zero. Samples containing pieces of fallout glass were wet-sieved in the field into size fractions and  
97 returned to the laboratory. For this study, individual glassy fallout samples were isolated from the  
98 1.4 to 1.7 mm size fractions by hand-picking using an optical microscope. Each piece of glassy fallout  
99 was inspected to characterize the color and general morphology (rounded edges and/or quasi-  
100 spherical shape; Fig. 1). Larger and smaller pieces of aerodynamic glasses, some with morphologies  
101 different from those studied here, were identified in other size fractions, but were not included in  
102 this study.

103

104 Optical images of fallout glass samples (Fig. 1) depict the most common morphologies observed in  
105 the 1.4 to 1.7 mm size fraction. Glass samples are typically opaque, greenish-black in color. Unlike  
106 trinitite, these glasses have smooth, rounded surfaces with no obvious top or basal surfaces. Quasi-  
107 spherical vesicles are often visible just beneath the smooth surfaces. Some glass samples appear to be  
108 fused agglomerations of many smaller glass quasi-spheres. All samples in this study appeared to be  
109 completely composed of glass, with no obvious crystalline features or visible compositional  
110 heterogeneities with the exception of variability in the density of adhered glass droplets and the  
111 density of vesicles. We classified glass morphologies as “quasi-spherical” or “oblong” based on their  
112 gross shapes. “Oblong” glasses, about twice as long or longer as they are wide, vary in shape from  
113 ovoid (Fig. 1, Panels C and E) to more irregular shapes difficult to categorize. Most “oblong”  
114 aerodynamic glasses have smooth, rounded surfaces that are often distorted by smaller glass droplet

115 features, and some “oblong” glasses appear to have a stretched morphology (Fig. 1, Panels D and F).  
116 “Quasi-spherical” aerodynamic glasses (Fig. 1, Panels A and B) approach spherical dimensions and  
117 tend to have few, if any, of the attached droplets prominent on the surfaces of most “oblong” glasses.  
118 Weathering rinds were not observed in these glasses (in contrast to the sediments, see below).

119

120 Glass samples were washed using 18.2 MΩ H<sub>2</sub>O, dried, and weighed using an XP2U ultra-  
121 microbalance (Mettler Toledo) with a precision of ±1 μg. The 28 fallout glass samples selected for  
122 analysis varied in mass from ~7 to 36 mg (Table 1).

123

124 *XRD and EDS-SEM characterization of sediments*

125

126 To determine the chemical and mineralogical composition of mineral constituents of the proximate  
127 sediments, the six sediment samples were analyzed using a Bruker D8 X-ray diffractometer (XRD).  
128 Powder mounts were prepared for XRD by crushing sediments in an agate mortar and pestle and  
129 loading the powders onto plastic mounts. Two samples (Sediment-3 and Sediment-4) were selected  
130 for additional analysis using a scanning electron microscope (SEM). Sediment grains were selected to  
131 account for the diversity of grain types visually observed in grab samples, although the grains of all  
132 samples appeared to consist predominantly of common silicate minerals like quartz and feldspar.  
133 Grains were mounted in epoxy and polished to expose the grain cores. The polished grain mounts  
134 were then coated with carbon and analyzed using an FEI Inspect F SEM fitted with an AMETEK EDAX  
135 Apollo XL energy-dispersive X-ray spectrometer (EDS). Secondary electron micrographs and  
136 backscattered electron micrographs (BSEM) were collected for 15-20 sediment grains on each grain  
137 mount. Chemical data were collected using the EDS system. Typically, 10-15 spot analyses were  
138 performed on each sediment grain to aid in mineral identification, and to characterize the observed  
139 textural and mineralogical heterogeneity observed in BSEM.

140

141 Most sediment grains are polymineralic and contain a diversity of textures and compositions. These  
142 grains display a porphyritic texture characteristic of most volcanic rocks (large, isolated, mm-scale

143 crystals within an intergrown microcrystalline and/or glassy groundmass). The matrix of sediment  
144 grains generally consists of quartz, K-feldspar, plagioclase, and glass. Pumice fragments,  
145 characterized by porous texture and a microcrystalline to glassy rock matrix, are also observed.  
146 Pumice fragments tend to lack crystals larger than  $\sim 10 \mu\text{m}$ . Sediment grains show minimal  
147 weathering or hydrothermal alteration. Weathering rinds on the rims of sediment grains are  $< 5 \mu\text{m}$ ,  
148 when present.

149

150 *Sample processing and dissolution for chemical and isotopic analysis*

151 Several grams of each of the six sediment samples, consisting of hundreds of grains, were crushed  
152 and homogenized in an agate mortar and pestle. The mortar and pestle was cleaned after each  
153 sample by scrubbing repeatedly with pure  $\text{SiO}_2$  sand, isopropanol, and 18.2 M  $\text{H}_2\text{O}$ . Approximately  
154 100 mg of each crushed and homogenized sediment was then selected for subsequent dissolution.  
155 The fallout glass samples were not crushed prior to dissolution.

156

157 Crushed sediment aliquots and whole glass samples were digested in clean Teflon beakers using a  
158 2.5:1 mixture of concentrated  $\text{HNO}_3$  to concentrated HF. United States Geological Survey rock  
159 standards BCR and BHVO, used in this study as procedural standards to assess major element and  
160 actinide data accuracy, were dissolved alongside fallout and sediment samples using the same  
161 procedures. All acids used in this study were “ultra-trace” grade (Seastar Chemicals, Inc.), with U and  
162 Th concentrations  $< 0.05 \text{ pg/g}$ , and diluted with 18.2 M  $\text{H}_2\text{O}$ . Samples were heated for at least 24  
163 hours, until a white fluoride precipitate formed. At this point,  $\sim 1 \text{ mL}$  concentrated  $\text{HClO}_4$  was added  
164 to each beaker to dissolve the fluoride precipitate. Samples were then dried down, dissolved in 1 mL  
165 concentrated HCl, and dried down again. Finally, samples were dissolved in 6 mL 3 M HCl. Using this  
166 treatment, all samples were completely dissolved, with no residual solid fractions remaining. Masses  
167 were obtained for the 3 M HCl solutions (hereafter referred to as “stock solutions”). Subsequent  
168 analyses were performed on aliquots of these solutions.

169

170 *Major element analysis by quadrupole-ICPMS*

171 Aliquots of the stock solutions for 22 fallout glass samples and all six sediment samples were  
172 transferred to a separate set of clean Teflon beakers, dried down, and dissolved and dried down  
173 twice in concentrated HNO<sub>3</sub> to remove residual chloride. The precipitates were then dissolved in a  
174 solution of 2% HNO<sub>3</sub> containing 5 ng/g <sup>6</sup>Li, <sup>45</sup>Sc, <sup>115</sup>In, and <sup>209</sup>Bi for internal standardization of Q-  
175 ICPMS measurements. Major element (Na, Mg, Al, K, Ca, and Fe) compositions of sediment and glass  
176 samples were measured using a Thermo X-series quadrupole ICPMS. Concentrations were quantified  
177 using a matrix-matched calibration curve for the elements of interest. Intensities were corrected  
178 using the known concentrations of the internal standard spike and the external calibration standards.

179

#### 180 *Chemical separation and analysis of U, Th, and Pa*

181 Uranium concentrations and isotopic compositions were measured in chemically-purified aliquots of  
182 stock solutions using isotope dilution mass spectrometry (IDMS). Sample aliquots were spiked with  
183 an internally calibrated <sup>233</sup>U spike. Spiked aliquots of stock solutions were then dried down and  
184 dissolved twice in 100 µL concentrated HNO<sub>3</sub>. After the second HNO<sub>3</sub> dissolution, the precipitates  
185 were dissolved in ~1 mL 4 M HNO<sub>3</sub> for the first of two ion chromatography uranium separations.  
186 Poly-Prep columns with 1.8 mL resin reservoirs (Bio-Rad Laboratories) were loaded with ~1.8 mL U-  
187 TEVA ion exchange resin (Eichrom Technologies) and conditioned with ~10 mL 4 M HNO<sub>3</sub>. Samples  
188 were loaded onto the resin, and the resin was washed with ~5 mL 4 M HNO<sub>3</sub>, ~3 mL 9 M HCl, and ~4  
189 mL 5 M HCl to remove matrix elements, while U remained sorbed to the resin. Uranium was eluted by  
190 adding ~8 mL 0.1 M HCl. Eluates containing U were dried down and dissolved in 100 µL  
191 concentrated HCl twice, then dried down a third time and dissolved in ~1 mL 9 M HCl. Poly-Prep  
192 columns were loaded with ~1.8 mL AG-1 X8 (100-200 mesh) anion exchange resin (Bio-Rad  
193 Laboratories) and conditioned with ~10 mL 9 M HCl. Samples were loaded onto the resin, and the  
194 resin was washed with ~7 mL 9 M HCl to remove matrix elements, while U remained sorbed to the  
195 resin. Uranium was then eluted from the resin by adding ~8 mL 0.1 M HCl. Eluates containing U were  
196 dried down and dissolved twice in concentrated HNO<sub>3</sub>, dried down a third time, and dissolved in ~3  
197 mL 2 % HNO<sub>3</sub> for analysis by multi-collector inductively-coupled plasma mass spectrometry (MC-  
198 ICPMS).

199

200 Thorium concentration and isotopic composition was measured on chemically-purified aliquots of  
201 stock solutions by IDMS using a calibrated  $^{229}\text{Th}$  spike. A three-step ion-exchange procedure was  
202 used to separate Th from matrix elements. For the first step, spiked aliquots of stock solutions were  
203 dried down and dissolved twice in 100  $\mu\text{L}$  concentrated HCl, then dried down a third time. Sample  
204 precipitates were dissolved in 2 mL 9 M HCl. To oxidize the dissolved components of these solutions,  
205 25  $\mu\text{L}$  of concentrated  $\text{HNO}_3$  was added to each solution. Poly-Prep columns were loaded with  $\sim 1.8$   
206 mL AG-1 X8 (100-200 mesh) anion exchange resin, and the resin was conditioned with  $\sim 10$  mL 9 M  
207 HCl. Thorium does not sorb to AG-1 resin in 9 M HCl, so beakers were placed to collect Th. Samples  
208 were loaded onto the resin, and Th was eluted with  $\sim 7$  mL 9 M HCl. Samples were dried down and  
209 dissolved in 100  $\mu\text{L}$  concentrated  $\text{HNO}_3$  twice, then dried down a third time. Sample precipitates  
210 were dissolved in  $\sim 1$  mL 8 M  $\text{HNO}_3$  for the second Th separation step. Poly-Prep columns were  
211 loaded with  $\sim 1.8$  mL AG-1 X8 (100-200 mesh) resin, and the resin was conditioned with  $\sim 10$  mL 8 M  
212  $\text{HNO}_3$ . Samples were loaded onto the column, and Th sorbed to the resin in the 8 M  $\text{HNO}_3$  medium.  
213 The resin was rinsed with  $\sim 7$  mL 8 M  $\text{HNO}_3$  to remove matrix elements. Beakers were then placed  
214 below the columns to collect Th, which was eluted using  $\sim 2$  mL 9 M HCl, followed by  $\sim 6$  mL 0.1 M  
215 HCl + 0.005 M HF. Samples were dried down and dissolved twice in 100  $\mu\text{L}$  concentrated HCl, then  
216 dried down a third time and dissolved in  $\sim 1$  mL 9 M HCl with 25  $\mu\text{L}$  concentrated  $\text{HNO}_3$  added as an  
217 oxidizer. The third Th separation step was an exact repetition of the first separation step. The Th  
218 eluate collected from the third separation step was dried down and dissolved twice in concentrated  
219  $\text{HNO}_3$ , dried down a third time, and dissolved in  $\sim 3$  mL 2 %  $\text{HNO}_3$  + 0.005 M HF for analysis by MC-  
220 ICPMS.

221

222 Six glass samples (GE-F-1 through 6) and two sediment samples (Sediment-1 and -2) were chosen for  
223 Pa chemical separation and analysis by IDMS, performed following a procedure described by Eppich  
224 *et al.* (2013), and using  $^{233}\text{Pa}$  spike-2 (for fallout samples F-1 through -3) and  $^{233}\text{Pa}$  spike-3 (for  
225 fallout samples F-4 through -6, and the sediment samples) described therein. Protactinium was  
226 separated from matrix elements using a three-step procedure. First, samples were dissolved in 9 M

227 HCl + 25  $\mu$ L saturated  $H_3BO_3$  + 50  $\mu$ L concentrated  $HNO_3$  and loaded onto Poly-Prep columns  
228 containing  $\sim$ 1.8 mL AG-1 X8 (100-200 mesh) resin conditioned with  $\sim$ 10 mL 9 M HCl. The resin was  
229 washed with  $\sim$ 7 mL 9 M HCl to remove matrix elements, and Pa was eluted with  $\sim$ 8 mL 9 M HCl +  
230 0.05 M HF. Samples were dried down after the addition of  $\sim$ 25  $\mu$ L concentrated  $HClO_4$  and dissolved  
231 in 2 %  $HNO_3$  + 25  $\mu$ L saturated  $H_3BO_3$ . Poly-Prep columns were loaded with  $\sim$ 1.5 mL clean quartz  
232 wool, which served as the separation medium for the second and third separation steps. The quartz  
233 wool was conditioned with  $\sim$ 10 mL 2 %  $HNO_3$ , samples were loaded onto the wool, and the wool was  
234 washed with  $\sim$ 7 mL 2 %  $HNO_3$ . Protactinium formed a hydrolyzed compound that sorbed to  $SiO_2$ ,  
235 while matrix elements washed through. To elute Pa,  $\sim$ 6 mL 2 %  $HNO_3$  + 0.05 M HF was added to each  
236 column. Samples were dried down after the addition of  $\sim$ 25  $\mu$ L concentrated  $HClO_4$ , and the  
237 precipitates were dissolved in 2 %  $HNO_3$  + 25  $\mu$ L concentrated  $HNO_3$ . The final Pa separation step  
238 was a repetition of the quartz wool technique, except Pa was eluted using  $\sim$ 3 mL 2 %  $HNO_3$  + 0.005  
239 M HF.

240

241 The spiked and chemically-purified aliquots of U, Th, and Pa were measured by MC-ICPMS. Uranium  
242 and Th analyses were performed following the analytical procedures outlined by Williams and  
243 Gaffney (2011), and Pa analyses were performed following the procedures outlined by Eppich *et al.*  
244 (2013). Uranium was measured using a Nu Plasma MC-ICPMS (aerodynamic glass samples F-1  
245 through -6) and a MicroMass IsoProbe MC-ICPMS (sediment samples and aerodynamic glass samples  
246 F-7 through -28). A static routine was used for Nu Plasma analyses, with  $^{238}U$  and  $^{235}U$  measured on  
247 Faraday detectors and  $^{236}U$ ,  $^{234}U$ , and  $^{233}U$  measured on ion counters. For analyses performed using  
248 the IsoProbe, fitted with a single ion counter, two separate runs were performed for each sample to  
249 obtain all of the necessary U isotopic ratios. In the first run,  $^{238}U$ ,  $^{235}U$ , and  $^{233}U$  were measured on  
250 Faraday detectors and  $^{234}U$  was measured on the ion counter, and in the second run  $^{238}U$ ,  $^{235}U$ , and  
251  $^{233}U$  measured on Faraday detectors and  $^{236}U$  was measured on the ion counter. Thorium and Pa  
252 were measured using a Nu Plasma MC-ICPMS. Thorium was measured using a static routine with  
253  $^{232}Th$  and  $^{229}Th$  measured on Faraday detectors and  $^{230}Th$  measured on an ion counter. Protactinium  
254 was measured using a static routine with  $^{233}Pa$  and  $^{231}Pa$  both measured on ion counters. Mass bias

255 correction factors and Faraday-ion counter gain factors were determined by measuring a solution of  
256 the NBL U-010 uranium isotopic standard spiked with a calibrated concentration of  $^{233}\text{U}$ . The  $^{233}\text{U}$ -  
257 spiked U-010 standard was analyzed every three to four analyses of unknowns. The measured  
258 isotopic composition of the  $^{233}\text{U}$ -spiked U-010 standards was used to determine mass bias correction  
259 factors and Faraday-ion counter gain factors for all U, Th, and Pa analyses.

260

261 For U and Th analyses, isotopic composition and isotope dilution measurements were performed on  
262 the same spiked aliquot of purified stock solution. A spike-stripping calculation was performed to  
263 subtract  $^{238}\text{U}$ ,  $^{236}\text{U}$ ,  $^{235}\text{U}$ , and  $^{234}\text{U}$  contributed by the spike from the signal intensity of those isotopes  
264 present in the sample. The contribution of  $^{230}\text{Th}$  and  $^{232}\text{Th}$  from the  $^{229}\text{Th}$  spike is insignificant, and  
265 no spike-stripping calculation was performed to correct the isotopic composition of  $^{229}\text{Th}$ -spiked  
266 samples. The  $^{233}\text{Pa}$  spike was produced by decay of  $^{237}\text{Np}$  and has virtually no  $^{231}\text{Pa}$  (Eppich *et al.*,  
267 2013), and no spike-stripping calculation was performed for Pa analyses.

268

## 269 **Results**

### 270 *Chemical composition results*

271 The major oxide constituents of the six nominally uncontaminated sediments are  $\text{Na}_2\text{O}$  (~3.6 wt. %),  
272  $\text{MgO}$  (~0.3 wt. %),  $\text{Al}_2\text{O}_3$  (~10.4 wt. %),  $\text{K}_2\text{O}$  (~4.5 wt. %),  $\text{CaO}$  (~1.5 wt. %), and  $\text{FeO}$  (~2.2 wt. %),  
273 consistent with a rhyolitic bulk chemical composition. Although  $\text{SiO}_2$  was not measured directly by  
274 ICPMS, it was determined by difference relative to the other major elements (calculated as the most  
275 common oxide) to be ~72 to 75 wt. %, and was confirmed by semi-quantitative X-ray fluorescence  
276 analysis. Sediment grains consist of common igneous mineral phases, particularly quartz, plagioclase  
277 feldspar, and K-feldspar (Fig. 2). Fe-Ti-rich mineral grains, also present in abundance, are easily  
278 identifiable in BSEM on the basis of high mean atomic number, morphology, and major element  
279 composition. Most sediment grains contain at least 1 vol. % of  $<10\ \mu\text{m}$  Fe-Ti-rich grains, although a  
280 few sediment grains have Fe-Ti-rich grains of larger sizes and abundances. A small fraction ( $<5\%$ ) of  
281 Fe-Ti-rich mineral grains contain a Mn-rich component.

282

283 Major element concentrations of the fallout glasses are presented in Table 1. The glasses are broadly  
284 similar to each other in bulk chemical composition. However, they do not have identical  
285 compositions, and vary in some elements more than others. For example, fallout glasses exhibit  
286 ~50% variation in CaO (calculated as the  $2\sigma$  standard deviation of 22 droplets); MgO and K<sub>2</sub>O  
287 concentrations also exhibit variation of 22.2 and 20.7 %, respectively. In contrast, Na<sub>2</sub>O, Al<sub>2</sub>O<sub>3</sub>, and  
288 FeO vary less than the other major elements, differing by 10.6, 7.5, and 8.9 %, respectively. The sum  
289 of the major elements (calculated as oxides) measured in glasses in this study is 24.33 wt. %, on  
290 average. The bulk of the remaining mass is SiO<sub>2</sub> (~72 to 75 wt. %), confirmed in SEM/EDS analyses of  
291 other fallout glasses from this population (Lewis, 2012).

292

293 To aid a comparison of glass and sediment compositions, the ratios of the elemental compositions of  
294 individual glass samples divided by the average of six sediment compositions were calculated (Table  
295 2). Glasses are almost identical to sediments in K<sub>2</sub>O concentrations, but are enriched in MgO relative  
296 to sediment by a factor of 1.3 to 2.0. Glasses are slightly enriched in Al<sub>2</sub>O<sub>3</sub> relative to sediments, by a  
297 factor of 1.02 to 1.16. Na<sub>2</sub>O is consistently depleted in glasses relative to sediments, up to a factor of  
298 0.86. CaO is variable in the glasses, as 7 of 22 glass samples are depleted in CaO relative to sediment,  
299 while the remaining are enriched, with sample F-12 the most enriched, by a factor of two. FeO is  
300 enriched in glasses relative to sediment by a factor of 1.2 to 1.5.

301

### 302 *Actinide composition results*

303 Uranium, Th, and Pa concentrations and isotopic compositions of fallout glasses and sediments are  
304 presented in Table 3. Five of the six sediment samples have uranium isotopic compositions within  
305 uncertainty of natural uranium ( $^{235}\text{U}/^{238}\text{U} = 7.2549 \times 10^{-3}$ ; Richter et al., 2010; Hiess *et al.*, 2012).  
306 Sediment-1 has a  $^{235}\text{U}/^{238}\text{U}$  ratio of  $0.01652 \pm 0.00002$ , about a factor of 2.3 higher than natural  
307 uranium. This sediment sample also has a  $^{234}\text{U}/^{238}\text{U}$  ratio about a factor of two higher than the other  
308 sediments, as well as detectable  $^{236}\text{U}$  ( $^{236}\text{U}/^{238}\text{U} = (4.50 \pm 0.03) \times 10^{-5}$ ), a nuclide that does not occur  
309 naturally in any significant abundance. The anomalous uranium isotopic composition of Sediment-1  
310 is attributed to the presence of micro-scale contamination from fallout. The five uncontaminated

311 sediments vary in uranium concentration from 2.7 to 4.8  $\mu\text{g/g}$  (average = 3.5  $\mu\text{g/g}$ ) and in  $^{234}\text{U}/^{238}\text{U}$   
312 from  $5.10 \times 10^{-5}$  to  $1.48 \times 10^{-4}$  (average =  $7.18 \times 10^{-5}$ ). None of the five uncontaminated sediment  
313 samples have  $^{236}\text{U}$  concentrations above the detection limit ( $\sim 4$  parts per trillion in solution).  
314 Sediment Th concentration varies from 21.1 to 24.8  $\mu\text{g/g}$ , and sediment  $^{230}\text{Th}/^{232}\text{Th}$  varies from  $(1.85$   
315  $- 3.48) \times 10^{-6}$ . The heterogeneity in  $^{230}\text{Th}/^{232}\text{Th}$  is attributed to differences in parent rock formation  
316 ages, initial  $^{230}\text{Th}/^{232}\text{Th}$  ratios, and ingrowth of  $^{230}\text{Th}$  from the decay of  $^{234}\text{U}$ . The two sediment  
317 samples measured for Pa yielded concentrations of 0.80 and 0.94  $\text{pg/g}$ .

318

319 Fallout glass samples vary in uranium concentration from 14.7 to 32.8  $\mu\text{g/g}$  (average = 23.6  $\mu\text{g/g}$ ), a  
320 factor of 3 to 12 higher than sediments. Fallout glass  $^{235}\text{U}/^{238}\text{U}$  is over two orders of magnitude  
321 higher than natural uranium, varying from 2.32 to 7.72 (average = 5.62). Fallout glass  $^{234}\text{U}/^{235}\text{U}$   
322 ratios are 0.01078 to 0.01093 (average = 0.0610), over two orders of magnitude higher than in  
323 sediment. All fallout glass samples analyzed in this study have measurable  $^{236}\text{U}$  concentrations;  
324  $^{236}\text{U}/^{238}\text{U}$  varies from 0.01161 to 0.0379 (average = 0.0275). Thorium concentrations in fallout  
325 glasses vary from 18.9 to 26.8  $\mu\text{g/g}$  (average = 23.5  $\mu\text{g/g}$ ), within the range of sediment Th  
326 concentrations and  $^{230}\text{Th}/^{232}\text{Th}$  ratios vary from  $(3.66 - 4.89) \times 10^{-6}$  (average =  $4.25 \times 10^{-6}$ ), about a  
327 factor of two higher than in the sediments. Protactinium concentrations from six fallout glasses vary  
328 from 1.82 to 2.45  $\text{pg/g}$  (average = 2.15  $\text{pg/g}$ ), about a factor of two higher than that observed in the  
329 sediments.

330

### 331 **Discussion**

#### 332 *Agglomeration and partial homogenization of fallout glasses during formation*

333 The fallout glasses examined here are the vitrified remnants of melted silicates that incorporated  
334  $^{235}\text{U}$  from nuclear fuel that was vaporized by the detonation but did not undergo fission ('residual  
335 fuel'). Fallout glasses yield major element compositions similar to, but not identical to, sediments  
336 collected from near ground zero, strongly suggesting that chemical composition of the fallout glass is  
337 primarily controlled by the composition of local sediments. The incorporation of bomb debris must  
338 have occurred between the time of sediment melting and subsequent quenching to a glass. These

339 findings are consistent with conclusions from studies of glasses formed during the Trinity event (e.g.,  
340 Fahey *et al.*, 2010). The striking compositional similarity of the fallout glasses and proximate  
341 sediments strongly suggests any chemical changes occurring over the timescale of fallout formation  
342 are second-order processes.

343

344 Although glasses and sediments are compositionally similar, there are some notable differences. The  
345 enrichments in MgO and FeO, as well as the depletion in Na<sub>2</sub>O in the fallout glasses relative to the  
346 sediments reflects a compositional change during fallout formation. This finding is consistent with  
347 the expected differences in volatility between the major elements, with Na being the most volatile. If  
348 the depletion in Na is due to volatilization, fallout must have been held at temperatures greater than  
349 the boiling point of Na<sub>2</sub>O (boiling point = 1950°C, ref?) for significant duration. Such conclusions,  
350 however, are dependent the following assumptions: 1) volatilization of SiO<sub>2</sub> did not occur (resulting  
351 in the loss of a chemical constituent not directly measured in fallout glass in this study); and 2) the  
352 six sediment samples measured in this study are truly representative of the initial chemical  
353 compositions of the melts. If temperatures exceeding the boiling point of the major elements (as  
354 oxides) were maintained for significant lengths of time (i.e., greater than of order seconds), the most  
355 volatile elements would have been lost to the vapor phase. Fallout glass morphologies confirm these  
356 materials solidified while airborne, and could not have been molten for longer than their time spent  
357 in flight. Recent work using stable noble gases (*Cassata et al.*, submitted) confirms that the formation  
358 time scales for glassy fallout debris are of order seconds.

359

360 No significant compositional differences between aerodynamic glasses characterized as “oblong” and  
361 “quasi-spherical” are observed, supporting that there is no difference between the chemical  
362 compositions of the two classes of fallout glass morphologically categorized here. Although CaO  
363 varies significantly more than the other major oxides (by about a factor of two), this variation is  
364 independent of morphology. The major element chemical heterogeneity strongly suggests that some  
365 degree of heterogeneity, initially present in the sediment, is retained during fallout formation, and

366 mixing resulting in compositional homogenization is not able to proceed to completion before  
367 solidification.

368

369 While most of the fallout glasses studied here preclude formation as direct condensates on the basis  
370 of size and time constraints, formation mechanisms involving both the melting and resolidification of  
371 bulk sediment particles, as well as the agglomeration of many smaller melt droplets (and, as a  
372 volumetrically minor contribution, condensates) prior to solidification are consistent with the lack of  
373 large major element compositional variations in aerodynamic glass samples. If this model is correct,  
374 the compositional range of individual small melt droplets adhering to larger, aerodynamically-  
375 shaped materials might be expected display a wider compositional range than the host. Size-based  
376 chemical investigations as well as micro-scale chemical analyses are needed to assess the degree of  
377 chemical homogenization recorded in both “quasi-spherical” and “oblong” aerodynamic fallout  
378 glasses to validate this hypothesis.

379

#### 380 *Two-component mixing of uranium in fallout glass*

381 The positive correlation between uranium concentration and  $^{235}\text{U}/^{238}\text{U}$  can only be explained by the  
382 incorporation of enriched remnant uranium from the device into fallout (Fig. 3). Uranium isotopic  
383 ratios in glasses also yield positive correlations between  $^{235}\text{U}/^{238}\text{U}$  and  $^{234}\text{U}/^{238}\text{U}$ , and between  
384  $^{235}\text{U}/^{238}\text{U}$  and  $^{236}\text{U}/^{238}\text{U}$  (Fig. 4). These correlations are best explained by two-component mixing,  
385 with naturally-occurring uranium in sediment and remnant fuel from the device as end-members.  
386 The sediment samples measured in this study have U-isotope compositions agreeing within error  
387 with the composition of the low- $^{235}\text{U}$  end-member suggested by the observed trends. The high- $^{235}\text{U}$   
388 end-member, residual fuel, was not sampled directly in this study. Glass sample F-25, the most  
389 highly-enriched sample measured in this study ( $^{235}\text{U}$  enrichment is  $88.54 \pm 0.09\%$ ), has a uranium  
390 isotope composition falling below the isotopic composition of uranium used in United States nuclear  
391 weapons (“oralloy”, ~93%). The device uranium end-member extrapolated from the correlations  
392 observed here, however, is likely not the same as the initial, pre-detonation isotopic composition of  
393 the fuel, due to partial fuel burn up in the detonation. The isotopic composition of uranium in fallout

394 has been affected by both fission and neutron reactions, in addition to mixing with natural uranium.  
395  $^{236}\text{U}$  is produced by neutron capture during fission, and may also be present in the uranium fuel. We  
396 cannot distinguish the relative contribution of  $^{236}\text{U}$  from these two sources using the current dataset.

397

398 Uranium from naturally-occurring sources has an essentially constant  $^{235}\text{U}/^{238}\text{U}$  ratio (Steiger and  
399 Jäger, 1977, Hiess *et al.*, 2012; although *cf.* Cowan and Adler, 1976; Brennecke *et al.*, 2010). In  
400 contrast, geological  $^{234}\text{U}/^{238}\text{U}$  ratios vary naturally, primarily due to preferential introduction of  $^{234}\text{U}$   
401 into meteoritic waters during weathering, due to alpha recoil of  $^{238}\text{U}$  (e.g. Kigoshi, 1971; Fleischer  
402 and Raabe, 1978). The five uncontaminated sediments analyzed here vary in  $^{234}\text{U}/^{238}\text{U}$  by about 18%.  
403 We ascribe this variation to hydrothermal alteration, not anthropogenic contamination. In this case,  
404 the naturally-occurring uranium end-member of the two-component mixing model is not constant in  
405 terms of  $^{234}\text{U}/^{238}\text{U}$ , and the mixing problem necessarily becomes a 3-component system. The  
406 remarkably coherent trend in  $^{235}\text{U}/^{238}\text{U}$  vs.  $^{234}\text{U}/^{238}\text{U}$ , however, suggests the presence of only two  
407 end-members. This result is due to the degree of enrichment of fallout glass in  $^{234}\text{U}$ , by over two  
408 orders of magnitude. Thus, fallout glass U-isotopic compositions are dominated by the contribution  
409 from anthropogenic uranium. Fallout glasses vary in  $^{234}\text{U}$  concentration from  $(2.83 - 7.92) \times 10^{14}$   
410 atoms/g, compared to the sediments, which vary in  $^{234}\text{U}$  concentration from  $(0.4 - 1.1) \times 10^{12}$   
411 atoms/g. The variation in  $^{234}\text{U}/^{238}\text{U}$  between the two end-members is much greater than the  
412 variation in  $^{234}\text{U}/^{238}\text{U}$  naturally occurring in sediments, obscuring the intrinsic variability in  
413  $^{234}\text{U}/^{238}\text{U}$  within sediment.

414

415 Natural uranium has a  $^{236}\text{U}/^{238}\text{U}$  ratio of  $<1 \times 10^{-9}$  (Zhao *et al.*, 1994) due to the short half-life of  $^{236}\text{U}$   
416 ( $2.348 \times 10^7$  years) relative to the age of the Earth, and production from parent nuclides ( $^{236}\text{Pa}$ ,  $^{236}\text{Np}$ ,  
417 and  $^{240}\text{Pu}$ ) that do not occur naturally. The  $^{236}\text{U}$  in fallout must therefore originate from  $^{236}\text{U}$  pre-  
418 existing in the device and/or produced during the detonation. Thus, best-fit line on a  $^{236}\text{U}/^{238}\text{U}$  versus  
419  $^{235}\text{U}/^{238}\text{U}$  plot with natural uranium as one end-member is expected to have a y-intercept within  
420 uncertainty of zero (sediment uranium end-member). We observe this relationship in the fallout  
421 glasses. The consistency of the relationship between  $^{235}\text{U}/^{238}\text{U}$ ,  $^{234}\text{U}/^{238}\text{U}$ , and  $^{236}\text{U}/^{238}\text{U}$  provides

422 additional confidence that the two-component mixing model proposed here is accurate for this suite  
423 of samples.

424

425 The  $^{234}\text{U}/^{235}\text{U}$  and  $^{236}\text{U}/^{235}\text{U}$  (Fig. 5) isotope ratios of fallout glass samples fall within a restricted  
426 range, varying from  $\sim 0.01074$  to  $\sim 0.01103$  and from  $\sim 0.00480$  to  $\sim 0.00506$ , respectively. It is  
427 possible that the values of  $^{234}\text{U}/^{235}\text{U}$  and  $^{236}\text{U}/^{235}\text{U}$ , clearly dominated by the device-contributed  
428 component, are unique to this test. Additional work on fallout glasses generated from other tests  
429 could assess whether the  $^{234}\text{U}/^{235}\text{U}$  and  $^{236}\text{U}/^{235}\text{U}$  values are indeed unique to each test. This  
430 information could have forensic value for comparison to a database of fallout compositions, such as  
431 those produced during the U.S. test program.

432

433 Some fallout glass samples have  $^{234}\text{U}/^{235}\text{U}$  and  $^{236}\text{U}/^{235}\text{U}$  ratios that extend to higher values (Figure  
434 5). The fallout samples with highest  $^{234}\text{U}/^{235}\text{U}$  and  $^{236}\text{U}/^{235}\text{U}$  ratios differ outside of uncertainty of  
435 samples with the lowest ratios. Analyses performed by Nu Plasma MC-ICPMS in this study have  
436 smaller uncertainties than analyses by MicroMass IsoProbe MC-ICPMS. All six samples analyzed  
437 using the Nu Plasma overlap within uncertainty, and also overlap with most of the analyses  
438 performed using the IsoProbe. A few IsoProbe analyses, however, fall outside the uncertainty of the  
439 Nu Plasma analyses, towards higher values of  $^{236}\text{U}/^{235}\text{U}$  and  $^{234}\text{U}/^{235}\text{U}$ . It is unclear what process  
440 might cause  $^{234}\text{U}$  and  $^{236}\text{U}$  to be positively, if weakly, correlated in the fallout glass samples. These  
441  $^{234}\text{U}/^{235}\text{U}$  and  $^{236}\text{U}/^{235}\text{U}$  variations may possibly reflect differences in unburned fuel composition  
442 incorporated into fallout during the detonation. Additional high-precision analyses of  $^{234}\text{U}/^{235}\text{U}$  and  
443  $^{236}\text{U}/^{235}\text{U}$  ratios in fallout glasses could assess the extent over which fallout varies in  $^{234}\text{U}/^{235}\text{U}$  and  
444  $^{236}\text{U}/^{235}\text{U}$ .

445

446  *$^{234}\text{U}$ - $^{230}\text{Th}$  and  $^{235}\text{U}$ - $^{231}\text{Pa}$  model ages*

447 The  $^{234}\text{U}$ - $^{230}\text{Th}$  and  $^{235}\text{U}$ - $^{231}\text{Pa}$  chronometers, well-established in geochemistry for determining the  
448 ages of rocks and minerals, have recently been applied to analysis of nuclear forensics samples, such  
449 as highly-enriched uranium in nuclear fuel (LaMont and Hall, 2005; Varga and Surányi, 2007;

450 Williams and Gaffney, 2011; Eppich *et al.*, 2013) to determine production ages. As the half-lives of the  
 451 parent and daughter nuclides are constant, calculation of production age, the most recent date of  
 452 chemical purification (hereafter referred to as “model age”) is a function only of the molar ratio of the  
 453 daughter and parent nuclides. Model ages are calculated using Eq. 1,

454

$$455 \quad t = \frac{\ln(1-R(\lambda_D-\lambda_P)/(\lambda_P))}{(\lambda_P-\lambda_D)} \quad (\text{Equation 1})$$

456

457 where  $t$  is time,  $R$  is the parent to daughter atomic ratio, and  $\lambda_P$  and  $\lambda_D$  are the decay constants of the  
 458 parent and daughter nuclides, respectively. In forensic investigations of fuel-cycle materials, the  
 459 model age of a sample is usually interpreted as the age of the most recent purification of the parent  
 460 from the daughter in the fuel production process. In ideal cases, model ages calculated using the  $^{234}\text{U}$ -  
 461  $^{230}\text{Th}$  and  $^{235}\text{U}$ - $^{231}\text{Pa}$  chronometers can have analytical uncertainties of less than hundreds of days.  
 462 Here we evaluate whether these chronometers can be used to determine model ages of the final  
 463 purification date of unburned nuclear fuel in fallout accurately. Two inherent assumptions in the  
 464 calculation of these model ages are:

- 465 1. Concentrations of the daughter nuclides ( $^{230}\text{Th}$  and  $^{231}\text{Pa}$ , in these systems) following the  
 466 final purification event are negligible (initial  $^{230}\text{Th}$  and  $^{231}\text{Pa}$  concentration = 0), and
- 467 2. No loss and/or gain of parent or daughter nuclides occurred between the time of final  
 468 purification and the time of analysis (closed system behavior).

469

470 Calculated  $^{234}\text{U}$ - $^{230}\text{Th}$  and  $^{235}\text{U}$ - $^{231}\text{Pa}$  model ages for aerodynamic glasses are presented in Table 4 and  
 471 Figure 6. Model ages calculated using the  $^{234}\text{U}$ - $^{230}\text{Th}$  chronometer for glasses for twenty-eight glass  
 472 samples vary from 128.8 to 314 years before 2012 (the year of analysis), and model ages calculated  
 473 using the  $^{235}\text{U}$ - $^{231}\text{Pa}$  chronometer for six glass samples vary from 119 to 151 years before 2012.  
 474 Fallout glass samples dated using both chronometers (F-1 through -6) do not have concordant model  
 475 ages; in each case, the  $^{234}\text{U}$ - $^{230}\text{Th}$  model age is older than the  $^{235}\text{U}$ - $^{231}\text{Pa}$  model age. As United States  
 476 near-surface nuclear weapons testing was restricted to the years 1945 through 1973 (49 to 67 years

477 before 2012), the model ages calculated using these chronometers must be systematically inaccurate,  
478 suggesting the presence of additional daughter nuclides, and/or that the assumptions inherent in the  
479 model age calculations are not consistent with the constraints placed on fallout formation.

480

481 These observations offer useful insights, suggesting several processes at work. In this sample suite,  
482 fallout contains uranium from two sources: the sediment, and the device. Furthermore, we have  
483 shown that sediments near ground zero contain non-negligible concentrations of  $^{230}\text{Th}$  and  $^{231}\text{Pa}$ .  
484 Based on the model of fallout formation proposed above, the addition of daughter nuclides to the  
485 system can occur during multiple processes:

- 486 1. Ingrowth of daughter nuclides in the device fuel prior to detonation,
- 487 2. After the detonation, two-component mixing of daughter nuclides from the device with  
488 daughter nuclides from the sediment, and
- 489 3. After fallout solidification, ingrowth of daughter nuclides from the uranium in glass.

490

491 It has been suggested by previous studies (Williams and Gaffney, 2011; Eppich *et al.*, 2013) that  
492 incomplete uranium purification at the fuel fabrication stage produces model ages older than the  
493 actual purification dates. Device detonation causes the loss of  $^{235}\text{U}$  to fission and neutron capture, and  
494 may have an effect on  $^{234}\text{U}$  through neutron capture, as well. Chemical fractionation due to  
495 differences in relative volatilities between uranium and daughter nuclides may occur as U, Th, and Pa  
496 condense and become incorporated into melted sediments. The largest source of systematic bias,  
497 however, is the contribution of naturally-occurring daughter nuclides from sediment. These  
498 processes all preclude a simple interpretation of model ages; each process can result in model ages  
499 systematically offset from the actual ages of fuel production and fallout formation. Additional  
500 research could help address the importance of neutron reactions and chemical fractionation, such  
501 that this system might be utilized to understand variations and heterogeneities resulting from  
502 incomplete mixing of the environmental materials following detonation.

503

504 *Incomplete melt homogenization revealed by fallout glass  $^{230}\text{Th}/^{232}\text{Th}$  heterogeneity*

505 Despite the similarity in major element composition between glasses and sediments, fallout glass has  
 506 a  $^{230}\text{Th}/^{232}\text{Th}$  ratio about a factor of two higher than sediment (Fig. 7). The incorporation of uranium  
 507 from the device, and the ingrowth of  $^{230}\text{Th}$  from  $^{234}\text{U}$  decay, can explain anomalously high  $^{230}\text{Th}/^{232}\text{Th}$   
 508 ratios in the fallout glasses. As has been previously shown, incorporation of U from the device results  
 509 in the enrichment of  $^{235}\text{U}$  and  $^{234}\text{U}$  in glasses by over two orders of magnitude relative to  $^{234}\text{U}$  and  $^{235}\text{U}$   
 510 concentrations in sediment. Decay of  $^{234}\text{U}$  after solidification of these melts results in  $^{230}\text{Th}$  ingrowth.  
 511 The contribution of  $^{230}\text{Th}$  from the decay of  $^{234}\text{U}$  can be modeled using Eq. 2,

512

$$513 \quad n_{230} = \frac{\lambda_{234}}{\lambda_{230} - \lambda_{234}} n_{234}^0 (e^{-\lambda_{234}t} - e^{-\lambda_{230}t}) \quad (\text{Equation 2})$$

514

515 where  $t$  is time since fallout formation in years,  $n_{230}$  is the number of atoms of  $^{230}\text{Th}$  produced by the  
 516 decay of  $^{234}\text{U}$  in time  $t$ ,  $n_{234}^0$  is the initial number of atoms of  $^{234}\text{U}$ , and  $\lambda_{234}$  and  $\lambda_{230}$  are the decay  
 517 constants of  $^{234}\text{U}$  and  $^{230}\text{Th}$  in decays per year, respectively. Eq. 2 can also be written to model the  
 518 ingrowth of  $^{231}\text{Pa}$  from the decay of  $^{235}\text{U}$  by substituting in the molar concentrations and decay  
 519 constants of  $^{235}\text{U}$  and  $^{231}\text{Pa}$ . Because the time of fallout formation can be estimated in this case  
 520 (bounded by  $t = 49$  to  $67$  years, the timespan of United States near-surface nuclear weapons testing  
 521 since 2012) and the number of atoms of  $^{234}\text{U}$  is measured directly (the concentration of  $^{234}\text{U}$  will not  
 522 decrease significantly over the timespan of decades, so  $n_{234}^t \approx n_{234}^0$ ), the number of atoms of  $^{230}\text{Th}$   
 523 produced by  $^{234}\text{U}$  decay can be bounded using the minimum and maximum years over which decay  
 524 occurred,  $49$  and  $67$  years, respectively. Eq. 2 only models  $^{230}\text{Th}$  ingrowth, only. Due to the long half-  
 525 life of  $^{230}\text{Th}$  ( $t_{1/2} = 75,600$  years) relative to the time period of decades, decay of initial  $^{230}\text{Th}$  can be  
 526 ignored.

527

528 The fraction of  $^{230}\text{Th}$  produced by  $^{234}\text{U}$  decay after melt solidification can be subtracted from the  
 529 measured fallout  $^{230}\text{Th}$  concentration. Decay-corrected  $^{230}\text{Th}/^{232}\text{Th}$  ratios are calculated using the  
 530 decay-corrected concentration of  $^{230}\text{Th}$ , the measured concentration of  $^{232}\text{Th}$ , and values of  $t$  of  $49$   
 531 years and  $67$  years (Table 5). The corrected  $^{230}\text{Th}/^{232}\text{Th}$  ratios are still heterogeneous, but now fall

532 within the range of  $^{230}\text{Th}/^{232}\text{Th}$  ratios measured in the sediment samples for all but one glass sample  
533 (F-12, Fig. 7). The similarity between the corrected ratios and the sediment ratios is consistent with  
534 the model of aerodynamic glass formation presented in this study.

535

536 The  $^{230}\text{Th}/^{232}\text{Th}$  heterogeneity in glassy fallout independently suggests that the melted sediments are  
537 incompletely mixed before quenching. Surface sediments proximal to the test are rocky, poorly-  
538 weathered sediments, consisting primarily of silicate minerals with a range of formation ages from  
539 Quaternary sediments to Tertiary volcanics. The abundance of quartz and feldspar suggests that the  
540 sediments were derived from the erosion of igneous rocks, which would be expected to exhibit  
541 variable  $^{230}\text{Th}/^{232}\text{Th}$  ratios depending on age and initial Th isotopic composition of the magmas from  
542 which they crystallized; the minerals present in these sediments likely formed over the course of  
543 millions of years. Furthermore,  $^{230}\text{Th}/^{232}\text{Th}$  ratios of the sediments measured in this study clearly  
544 demonstrate a heterogeneous reservoir from which melt glass formed. The  $^{230}\text{Th}/^{232}\text{Th}$   
545 heterogeneity in fallout glasses demonstrates that the reservoir heterogeneity is maintained, and  
546 that, while chemical homogenization of sediments did occur, the process was not able to proceed to  
547 completion.

548

#### 549 *Sequence of events in fallout glass formation*

550 Utilizing the data presented here, we can reconstruct the sequence of events that led to the formation  
551 of the fallout glass samples examined in this study (Fig. 8). A nuclear device, containing uranium with  
552 a  $^{235}\text{U}$  enrichment greater than 88.5% (possibly "oralloy", ~93 %) and an unknown  $^{234}\text{U}/^{238}\text{U}$  and  
553  $^{236}\text{U}/^{238}\text{U}$  composition, was detonated in a near-surface test. A quantity of remnant fuel was  
554 vaporized along with other bomb-related proximate materials.  $^{236}\text{U}$  was generated during the chain  
555 reaction due to neutron capture on  $^{235}\text{U}$ . The rate at which the nuclear chain reaction occurred  
556 altered the isotopic composition of the residual fuel instantaneously relative to the timescale of  
557 fallout formation. It is unclear how the  $^{234}\text{U}$  and  $^{238}\text{U}$  initially present in the fuel were affected, and  
558 what initial  $^{236}\text{U}$  was present.

559

560 Within seconds of the explosion, vapor in the resultant debris cloud began to condense. Condensates  
561 were incorporated onto and into silicate melts formed from sediments swept into and heated by the  
562 fireball. Residual uranium fuel, dispersed by the explosion, mixed with naturally-occurring uranium.  
563 The mechanism for incorporation of the bomb debris into the silicate melts is not uniquely  
564 identifiable from this line of research, but must be the result of a combination of condensation,  
565 agglomeration, mixing, and diffusion. The presence of embedded quasi-spherical features (Fig. 1,  
566 Panels C-F) on fallout glasses supports that at least some aerodynamic glasses formed by coalescence  
567 of smaller melt droplets. Further work should be performed to examine the elemental distribution  
568 within fallout glasses on the micro-scale, with an emphasis on the identification of diffusion profiles  
569 and convective mixing to constrain the relative influence of different processes on the incorporation  
570 of the bomb debris into the melts.

571

572 The silicate melts became closed systems at the time of quenching, and mixing and homogenization  
573 ceased at this point. The debris-laden silicate melts quenched to glass before their combination of  
574 ballistic trajectories and gravitational effects deposited them on the surface, resulting in  
575 aerodynamic morphologies. If evaporative loss of major element sediment components occurred (e.g.  
576 volatilization of Na), it did not proceed to completion, as indicated by the compositional similarity of  
577 glasses and sediments. From the time of quenching to the time of sample collection and analysis, the  
578  $^{234}\text{U}$  and  $^{235}\text{U}$  in these glasses decayed and was retained in the glassy matrices, leading to the  
579 ingrowth of  $^{230}\text{Th}$  and  $^{231}\text{Pa}$ , respectively.

580

581 These results illustrate several insights into fallout formation: 1) The composition of the  
582 environmental materials in a near-surface nuclear explosion determine and dominate the  
583 concentrations of the major and most trace elements in resultant local fallout. Thus, understanding  
584 the interaction of different environmental materials with the debris cloud may improve  
585 interpretations or predictions of resultant fallout chemistry; 2) the timescales for fallout formation  
586 are short (~seconds), and the timing of sediment interaction in relation to the cooling rate of the  
587 fireball will strongly influence the degree of chemical homogenization occurring with respect to the

588 incorporation of remnant fuel; 3) droplets that remain molten for longer periods of time, perhaps  
589 due to their ballistic trajectories through the fireball, will have more time to homogenize initially  
590 variable compositions such that the range of heterogeneity observed should reflect a combination of  
591 yield and height of detonation; and 4) multiple physical processes must result in the introduction of  
592 bomb-debris condensates into the environmental melts that form the host material of macro-scale  
593 glassy fallout. While the fallout samples examined in this study cannot be the direct result of  
594 condensation from the bomb vapor, such fallout must have incorporated primary condensates, and  
595 this inventory dominates the uranium budget of these aerodynamic glasses. This suggests that such  
596 glassy fallout materials may be of high value for nuclear forensic investigations. These observations  
597 also highlight a need to understand the micro-scale features in these materials to deconvolve the  
598 formation processes of condensation, agglomeration, mixing, and diffusion. While the era of above-  
599 ground testing is over, studies of historical fallout continue to provide insight for hazard assessment  
600 as well as nuclear forensics.

601

## 602 **Acknowledgements**

603

604 The authors acknowledge Ross Williams for his invaluable guidance on actinide chemical separations  
605 and isotopic analyses. Rachel Lindvall and Zurong Dai are thanked for their instruction on and  
606 assistance with quadrupole ICPMS and SEM analyses, respectively. Bill Cassata, Stan Prussin and  
607 Brett Isselhardt provided useful comments that led to the improvement of the manuscript. This work  
608 performed under the auspices of the U.S. Department of Energy by Lawrence Livermore National  
609 Laboratory under Contract DE-AC52-07NA27344. This work was funded by the Laboratory Directed  
610 Research and Development Program at LLNL under project tracking code 13-ERD-062, as well as  
611 with support by the Office of Defense Nuclear Nonproliferation Research and Development within  
612 the U.S. Department of Energy's National Nuclear Security Administration. LLNL-JRNL-650394.

613

614

615

616

617

## **References**

- 618 Adams CE; Farlow NH; Schell WR. 1960. The composition, structures and origins of radioactive fall-  
619 out particles. *Geochimica et Cosmochimica Acta* 18, 42-56.  
620
- 621 Belloni F; Himbert J; Marzocchi O; Romanello V. 2011. Investigating incorporation and distribution of  
622 radionuclides in trinitite. *Journal of Environmental Radioactivity* 102, 852-862.  
623
- 624 Bellucci JJ; Simonetti A. 2012. Nuclear forensics: searching for nuclear device debris in trinitite-  
625 hosted inclusions. *Journal of Radioanalytical and Nuclear Chemistry* 293, 313-319.  
626
- 627 Bellucci JJ; Simonetti A; Wallace C; Koeman EC; Burns PC. 2013a. Isotopic fingerprinting of the  
628 world's first nuclear device using post-detonation materials. *Analytical Chemistry* 85, 4195-  
629 4198.  
630
- 631 Bellucci JJ; Simonetti A; Wallace C; Koeman EC; Burns PC. 2013b. Lead isotopic composition of  
632 trinitite melt glass: evidence for the presence of Canadian industrial lead in the first atomic  
633 weapon test. *Analytical Chemistry* 85, 7588-7593.  
634
- 635 Bellucci JJ; Wallace C; Koeman EC; Simonetti A; Burns PC; Kieser J; Port E; Walczak T. 2012.  
636 Distribution and behavior of some radionuclides associated with the Trinity nuclear test.  
637 *Journal of Radioanalytical and Nuclear Chemistry* 295, 2049-2057.  
638
- 639 Brennecka GA; Borg LE; Hutcheon ID; Sharp MA; Anbar AD. 2010. Natural variations in uranium  
640 isotope ratios of uranium ore concentrates: understanding the  $^{238}\text{U}/^{235}\text{U}$  fractionation  
641 mechanism. *Earth and Planetary Science Letters* 291, 228-233.  
642
- 643 Cassata WS; Prussin SG; Knight KB; Hutcheon ID; Isselhardt BH; Renne PR. 2013. When the dust  
644 settles: applications of stable xenon isotopes to nuclear forensics research.  
645
- 646 Cowan GA; Adler HH. 1976. The variability of the natural abundance of  $^{235}\text{U}$ . *Geochimica et*  
647 *Cosmochimica Acta* 40, 1498-1490.  
648
- 649 Eby N; Hermes R; Charnley N; Smoliga JA. 2010. Trinitite – the atomic rock. *Geology Today* 26, 181-  
650 186.  
651
- 652 Eppich GR; Williams RW; Gaffney AM; Schorzman KC. 2013.  $^{235}\text{U}$ - $^{231}\text{Pa}$  age dating of uranium  
653 materials for nuclear forensic investigations. *Journal of Analytical Atomic Spectrometry* 28,  
654 666-674.  
655
- 656 Fahey AJ; Zeissler CJ; Newbury DE; Davis J; Lindstrom RM. 2010. Post-detonation nuclear debris for  
657 attribution. *Proceedings of the National Academy of Sciences* 107, 20207-20212.  
658
- 659 Fleischer RL; Raabe OG. 1978. Recoiling alpha-emitting nuclei. Mechanisms for uranium-series  
660 disequilibrium. *Geochimica et Cosmochimica Acta* 42, 973-978.  
661
- 662 Glasstone S; Dolan PJ. 1977. *The Effects of Nuclear Weapons*. US DOD and US DOE. US Government  
663 Printing Office: 1977 O-213-794, Washington, DC.  
664
- 665 Hermes RE; Strickfaden WB. 2005. A new look at trinitite. *Nuclear Weapons Journal* 2, 2-7.  
666
- 667 Kigoshi K. 1971. Alpha-recoil thorium-234: dissolution into water and the uranium-234/uranium-  
668 238 disequilibrium in nature. *Science* 173, 47-48.  
669
- 670 LaMont SP; Hall G. 2005. Uranium age determination by measuring the  $^{230}\text{Th}/^{234}\text{U}$  ratio. *Journal of*  
671 *Radioanalytical and Nuclear Chemistry* 264, 423-427.  
672

- 673 Lewis L. 2012. *Characterizing the Distribution of Unfissioned Fuel in Quasi-Spherical Glasses Created by*  
674 *a Low-Yield Surface Nuclear Explosion*. M.S. Thesis. University of California – Berkeley: United  
675 States.  
676
- 677 Parekh PP; Semkow TM; Torres MA; Haines DK; Cooper JM; Rosenberg PM; Kitto ME. 2006.  
678 Radioactivity in trinitite six decades later. *Journal of Environmental Radioactivity* 85, 103-  
679 120.  
680
- 681 Steiger RH; Jäger E. 1977. Subcommittee on geochronology: convention on the use of decay  
682 constants in geo- and cosmochronology. *Earth and Planetary Science Letters* 36, 359-362.  
683
- 684 U.S. House of Representatives. 111th Congress. [H.R. 730], *Nuclear Forensics and Attribution Act*.  
685 Washington: Government Printing Office, 2010.  
686
- 687 Varga Z; Surányi G. 2007. Production date determination of uranium-oxide materials by inductively  
688 coupled plasma mass spectrometry. *Analytica Chimica Acta* 599, 16-23.  
689
- 690 Williams RW; Gaffney AM. 2011.  $^{230}\text{Th}$ - $^{234}\text{U}$  model ages of some uranium standard reference  
691 materials. *Radiochimica Acta* 1, 31-35.  
692
- 693 Zhao X-L; Nadeau M-J; Kilius LR; Litherland AE. 1994. The first detection of naturally-occurring  $^{236}\text{U}$   
694 with accelerator mass spectrometry. *Nuclear Instruments and Methods in Physics Research B*  
695 92, 249-253.  
696  
697

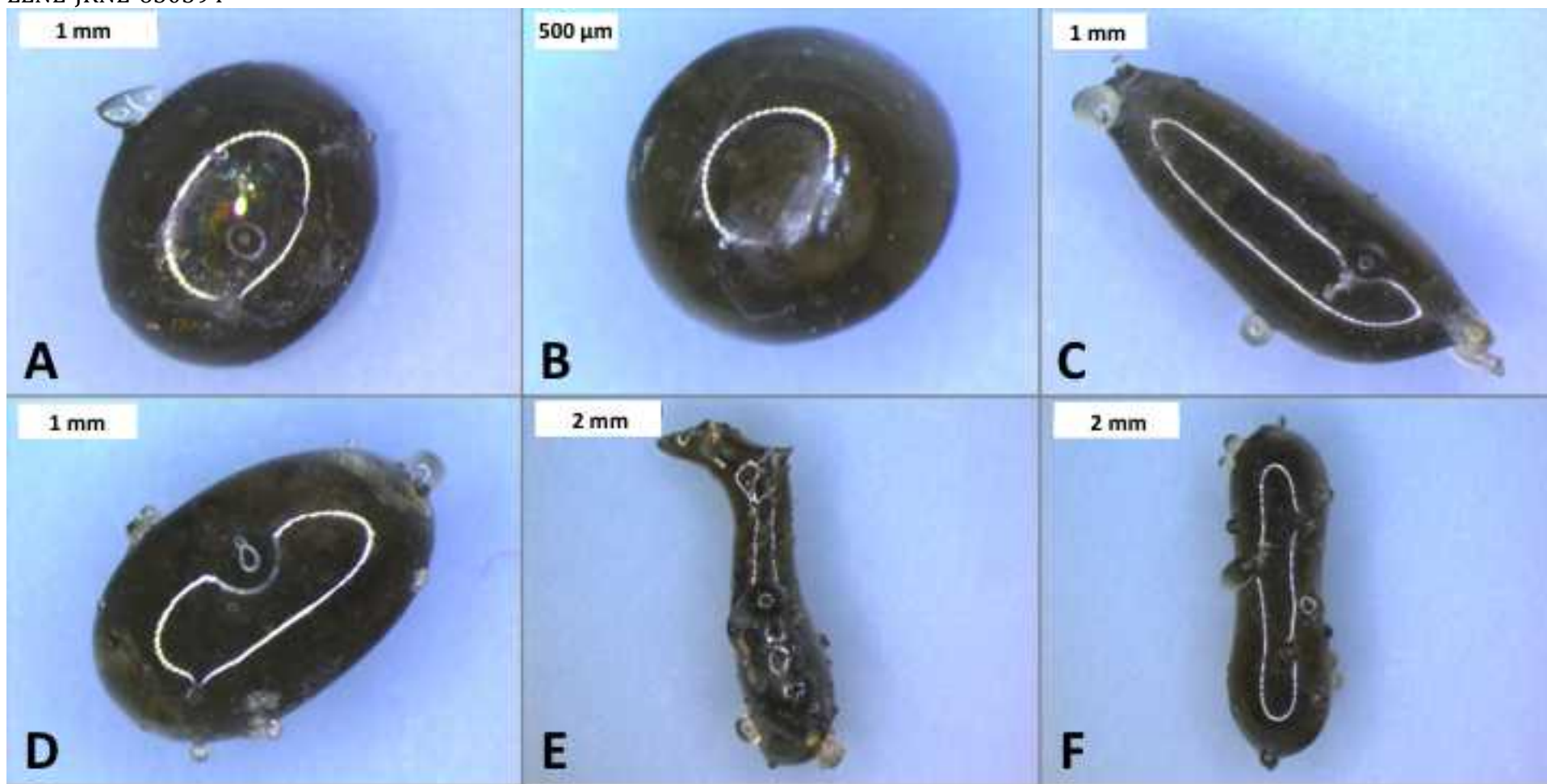


Figure 1. Optical microscope images of fallout glasses. Panels A and B are representative of samples in this study characterized as “quasi-spherical”, and Panels C-F are representative of samples characterized as “oblong”. Note the abundance of embedded quasi-spherical features on the “oblong” glass samples in Panels C-F.

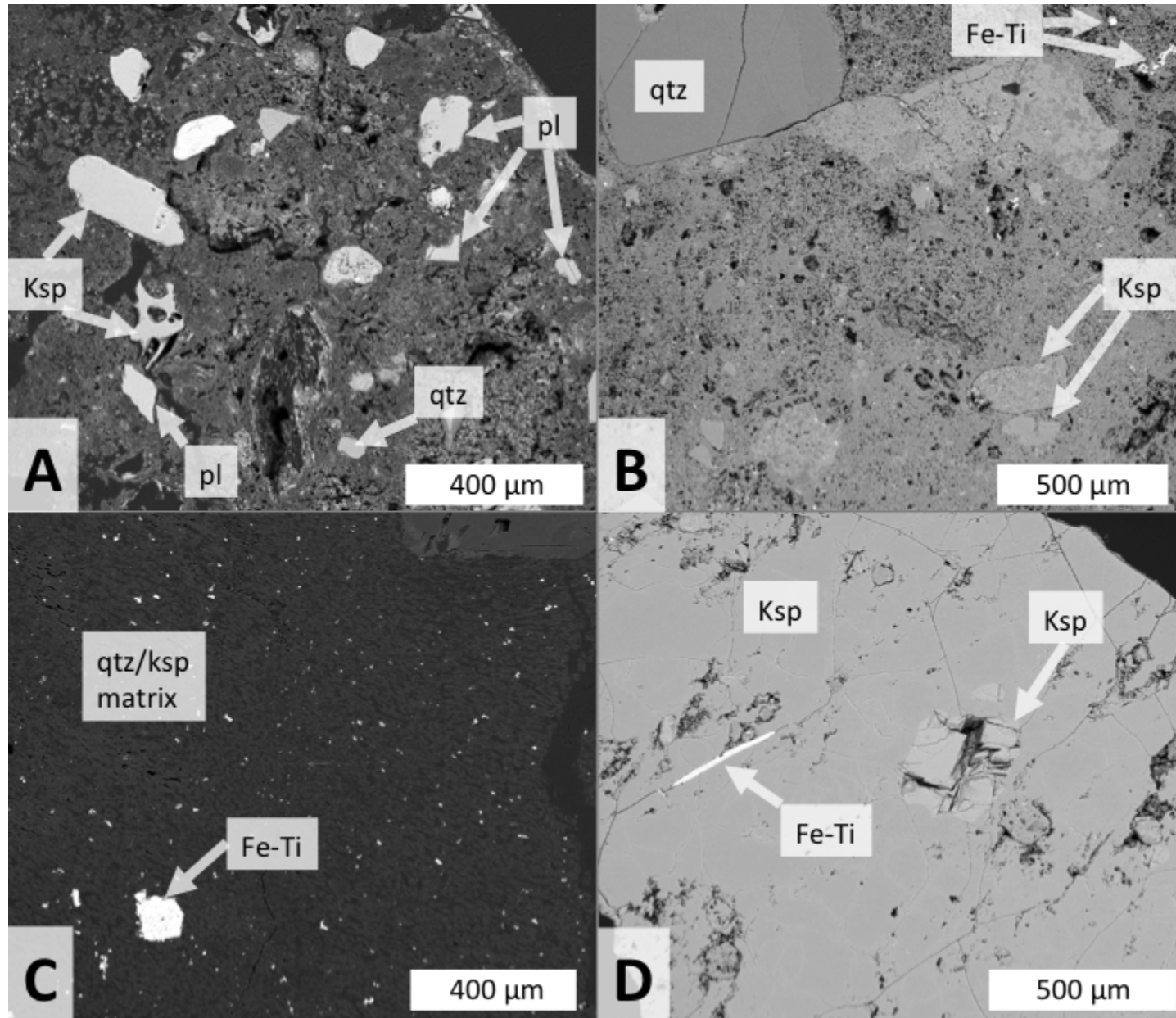


Figure 2. Backscattered electron micrograph images of polished sections of four sediment grains from Sediment-3. Mineralogy is determined on the basis of major element composition measured by spot analysis energy-dispersive X-ray fluorescence spectrometry (EDS). qtz, quartz; Ksp, potassium feldspar; pl, plagioclase; Fe-Ti, iron-titanium oxides.

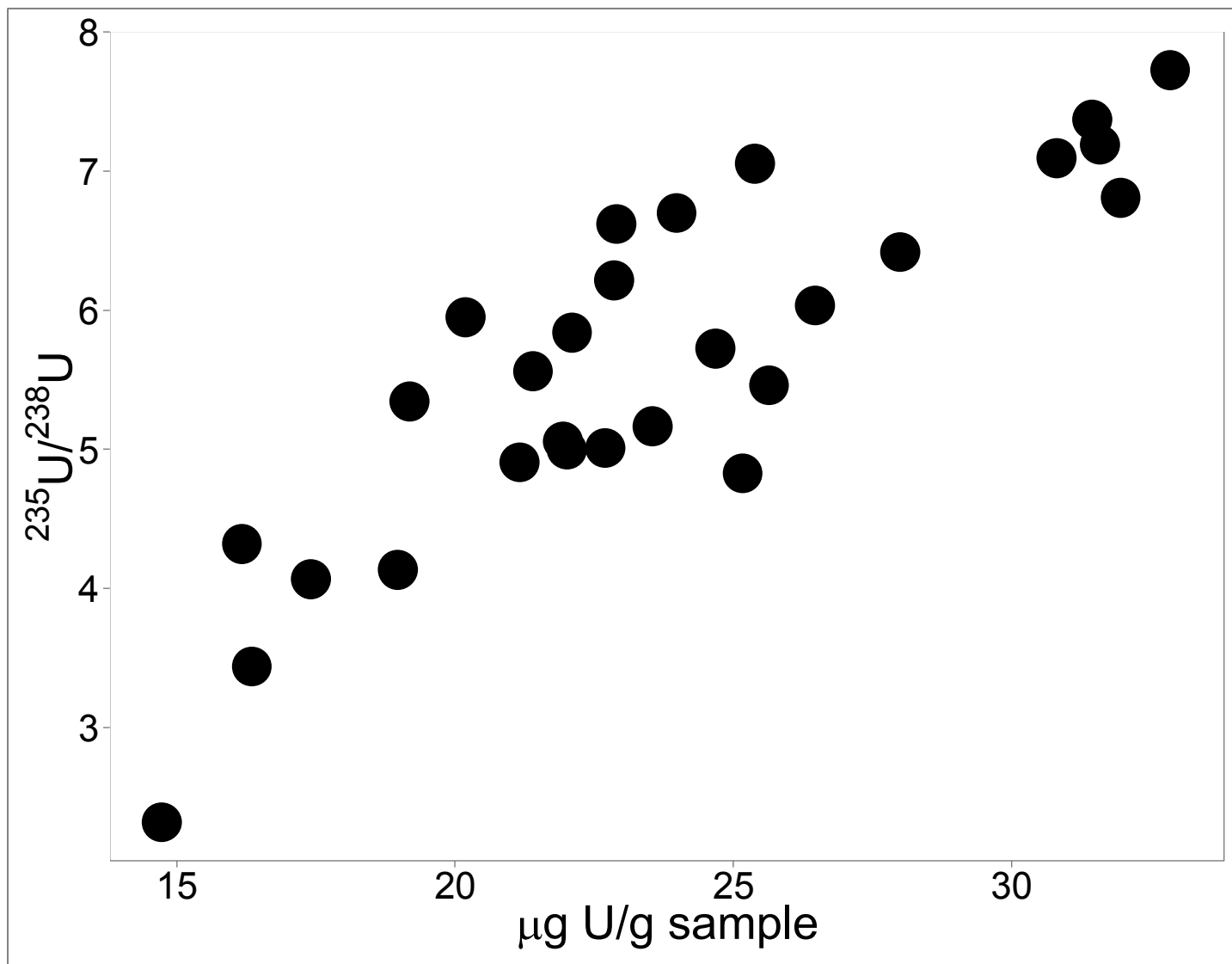


Figure 3. Uranium concentrations and isotopic compositions of fallout glass. Uncertainties are smaller than symbols.

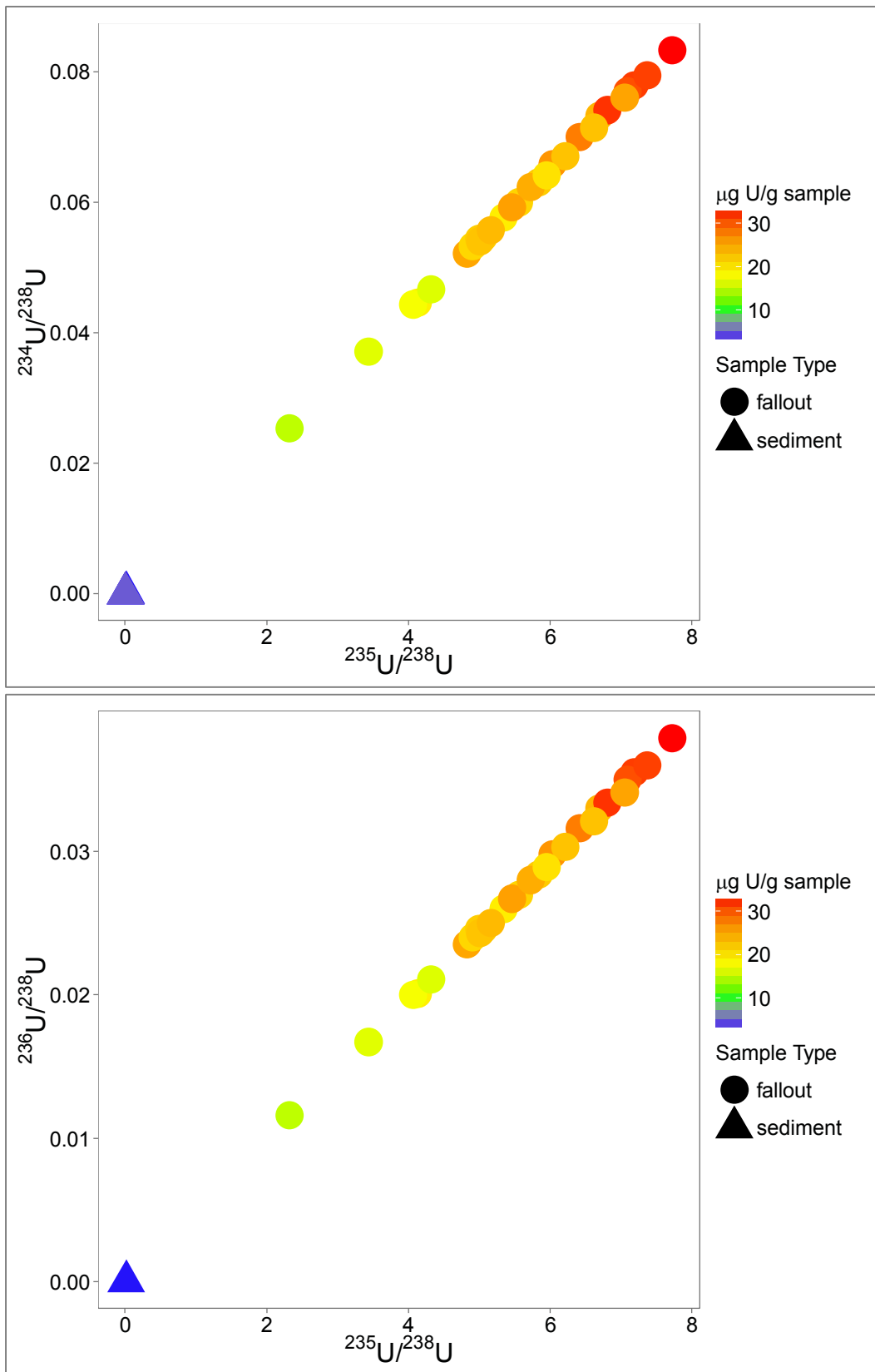


Figure 4. Uranium concentrations and isotopic compositions of fallout glasses and sediments. Sediment data points overlap in both panels, clustering within uncertainty of natural uranium near the origin ( $^{235}\text{U}/^{238}\text{U} \approx 0.00725$ ) and at ( $^{236}\text{U}/^{238}\text{U} \approx 0$ ). Uncertainties are smaller than symbols in both panels.

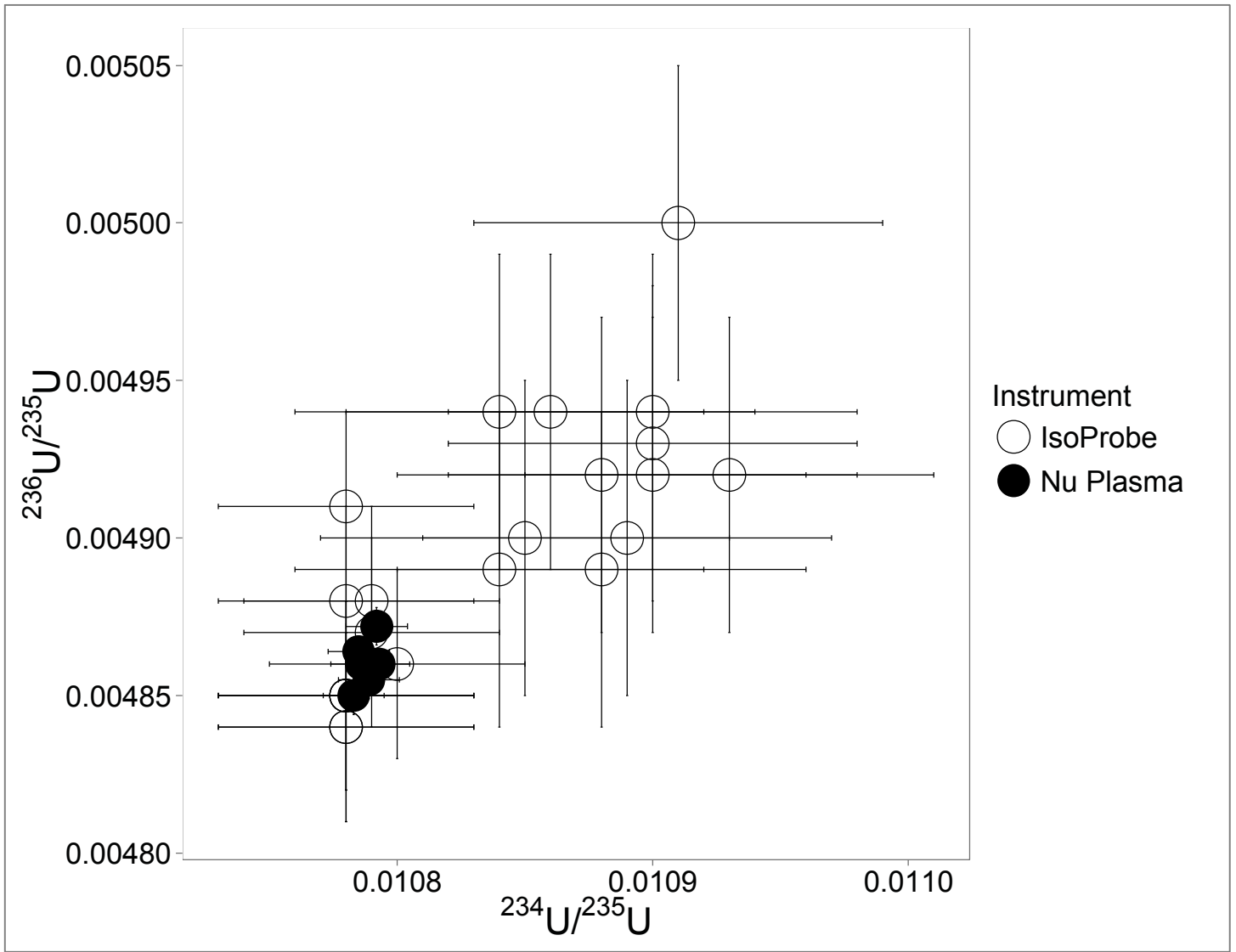


Figure 5.  $^{234}\text{U}/^{235}\text{U}$  versus  $^{236}\text{U}/^{235}\text{U}$  in fallout glasses, as measured using a Nu Plasma MC-ICPMS and a MicroMass IsoProbe MC-ICPMS.

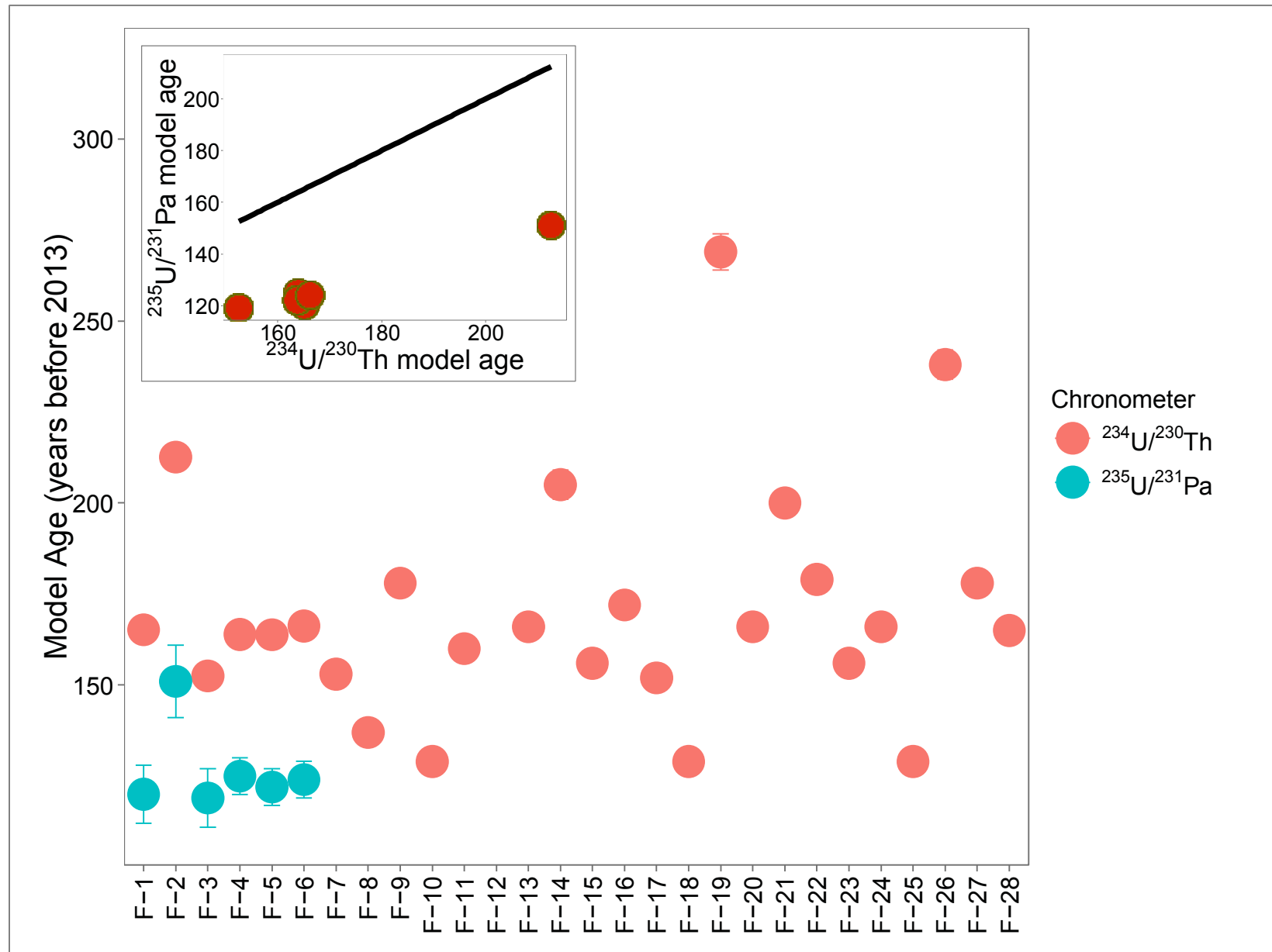


Figure 6. Fallout glass  $^{234}\text{U}$ - $^{230}\text{Th}$  and  $^{235}\text{U}$ - $^{231}\text{Pa}$  model ages. See Supplementary Table A for data used to calculate these ages. True possible ages of fallout are 49 to 67 years before 2012. Black line in inset is the line of equal  $^{234}\text{U}$ - $^{230}\text{Th}$  and  $^{235}\text{U}$ - $^{231}\text{Pa}$  model age. When not shown, model age uncertainties are smaller than symbols.

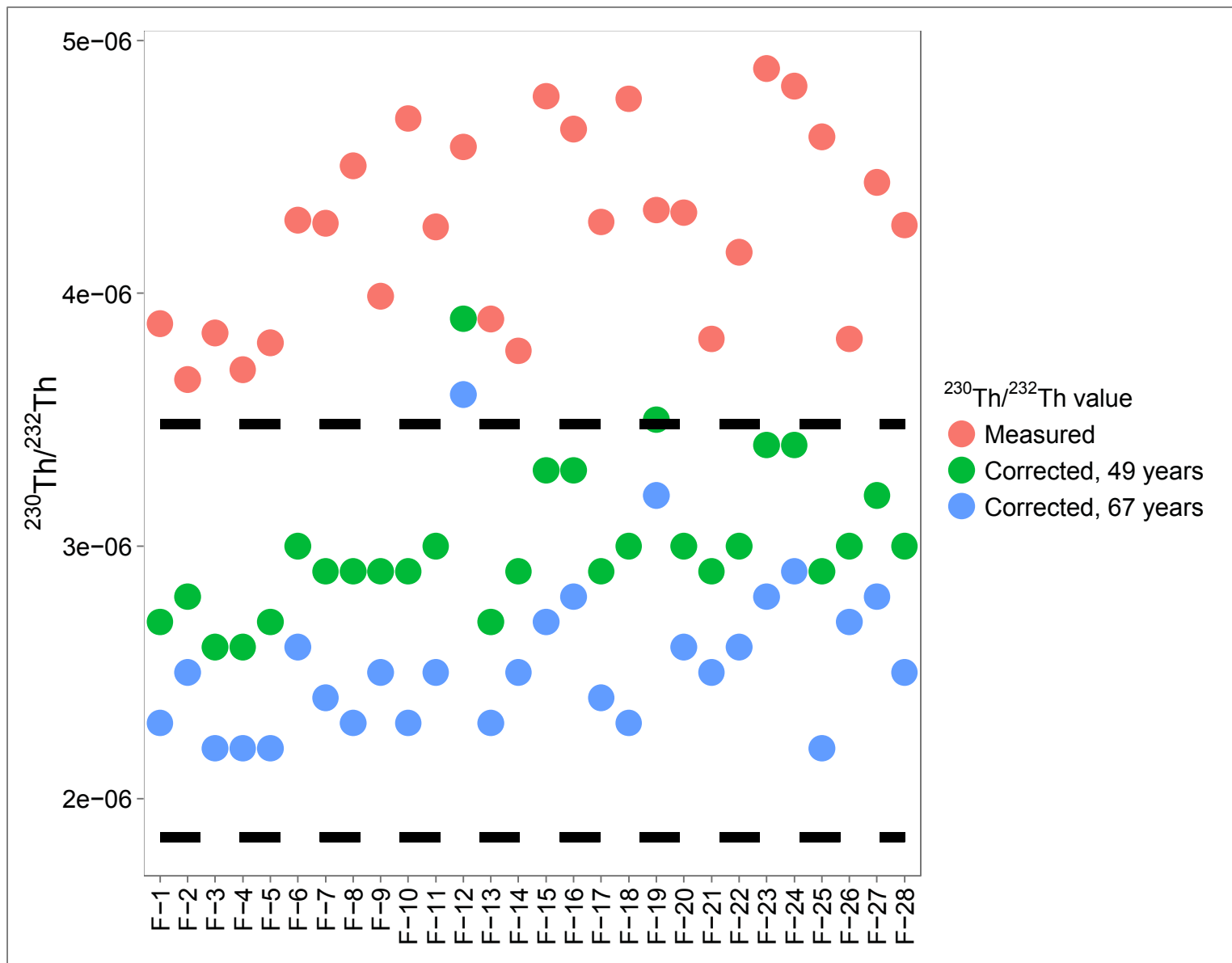


Figure 7. Fallout glass thorium isotopic compositions. Measured  $^{230}\text{Th}/^{232}\text{Th}$  values are plotted as red circles. Green and blue circles represent decay-corrected  $^{230}\text{Th}/^{232}\text{Th}$  values. Decay correction is performed using Equation 2, assuming  $t = 49$  years (blue circles) and  $67$  years (green circles), the minimum and maximum possible true ages of the fallout (see text). The region of  $^{230}\text{Th}/^{232}\text{Th}$  values bound by the black dotted lines represents the range of  $^{230}\text{Th}/^{232}\text{Th}$  values measured in six sediment samples. Uncertainties for “measured” data points are smaller than symbols.

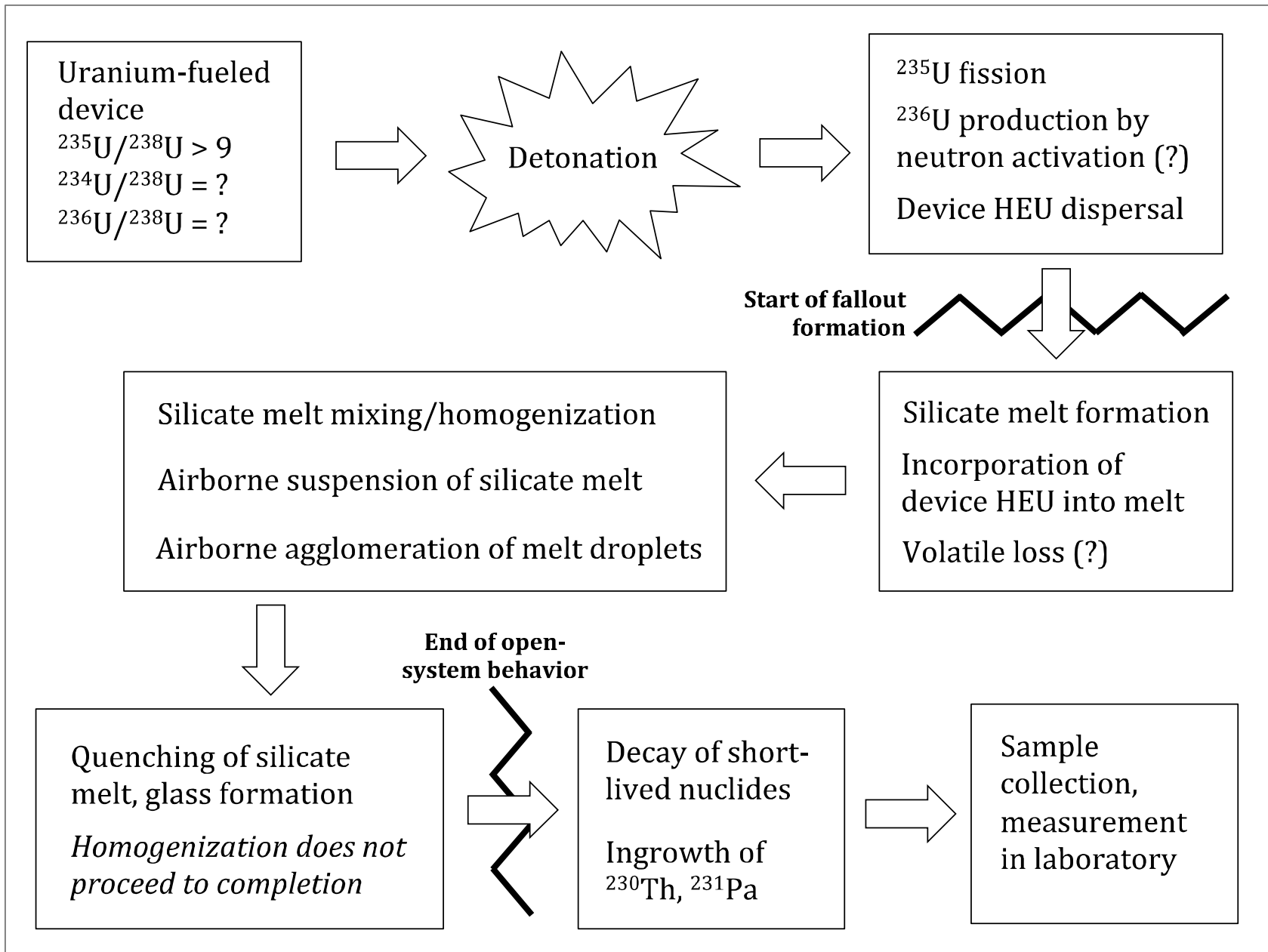


Figure 8. Flow chart depicting the sequence of events responsible for the formation of glassy fallout examined in this study. No time or length scale is implied by this figure.

Sample ID	Mass (g)	Shape	Na <sub>2</sub> O (wt. %)	uncert.	MgO (wt. %)	uncert.	Al <sub>2</sub> O <sub>3</sub> (wt. %)	uncert.	K <sub>2</sub> O (wt. %)	uncert.	CaO (wt. %)	uncert.	FeO (wt. %)	uncert.
<i>aerodynamic glasses</i>														
F-1	0.035600	oblong	NM	-	NM	-	NM	-	NM	-	NM	-	NM	-
F-2	0.030618	oblong	NM	-	NM	-	NM	-	NM	-	NM	-	NM	-
F-3	0.024565	oblong	NM	-	NM	-	NM	-	NM	-	NM	-	NM	-
F-4	0.027148	oblong	NM	-	NM	-	NM	-	NM	-	NM	-	NM	-
F-5	0.024625	oblong	NM	-	NM	-	NM	-	NM	-	NM	-	NM	-
F-6	0.024938	oblong	NM	-	NM	-	NM	-	NM	-	NM	-	NM	-
F-7	0.021116	oblong	3.52	0.11	0.61	0.02	11.2	0.3	4.35	0.13	1.72	0.07	3.05	0.15
F-8	0.017437	oblong	2.97	0.08	0.62	0.02	12.2	0.5	3.91	0.12	1.65	0.06	3.11	0.06
F-9	0.020327	oblong	3.32	0.05	0.624	0.012	11.34	0.15	4.18	0.12	1.93	0.04	3.11	0.09
F-10	0.017022	oblong	3.49	0.08	0.544	0.010	11.4	0.2	4.3	0.2	1.36	0.08	3.10	0.10
F-11	0.015143	oblong	3.25	0.09	0.614	0.005	11.34	0.15	4.20	0.11	1.75	0.07	3.04	0.14
F-12	0.018902	oblong	3.46	0.07	0.56	0.02	10.6	0.2	4.23	0.12	2.90	0.08	2.83	0.09
F-13	0.023776	oblong	3.32	0.11	0.536	0.010	10.6	0.2	4.05	0.12	2.27	0.08	2.89	0.10
F-14	0.019379	oblong	3.17	0.09	0.509	0.013	10.78	0.12	4.02	0.07	1.90	0.07	2.88	0.05
F-15	0.009058	quasi-spherical	3.07	0.09	0.642	0.013	11.38	0.15	4.36	0.08	1.54	0.04	3.07	0.10
F-16	0.008650	quasi-spherical	3.41	0.07	0.504	0.005	11.2	0.2	4.53	0.10	0.99	0.04	3.23	0.08
F-17	0.017236	oblong	3.13	0.15	0.594	0.012	11.6	0.2	4.05	0.08	1.90	0.04	3.01	0.03
F-18	0.018805	oblong	3.55	0.03	0.645	0.013	11.2	0.2	4.36	0.06	1.71	0.07	3.14	0.05
F-19	0.007086	quasi-spherical	3.40	0.13	0.605	0.012	11.2	0.2	4.99	0.18	1.78	0.06	3.06	0.09
F-20	0.010145	oblong	3.50	0.07	0.506	0.012	11.0	0.3	4.59	0.14	1.23	0.06	3.07	0.04
F-21	0.009069	quasi-spherical	3.09	0.07	0.489	0.015	11.1	0.2	4.96	0.17	1.15	0.03	2.95	0.06
F-22	0.011855	oblong	3.38	0.08	0.562	0.013	11.0	0.3	5.24	0.17	1.54	0.07	2.78	0.12
F-23	0.007955	quasi-spherical	3.15	0.13	0.60	0.02	12.1	0.3	5.25	0.11	1.68	0.06	2.96	0.10
F-24	0.007408	quasi-spherical	3.17	0.12	0.650	0.008	11.7	0.3	5.48	0.17	1.44	0.11	2.97	0.08
F-25	0.012177	oblong	3.33	0.08	0.531	0.010	11.2	0.2	4.78	0.11	1.41	0.07	2.91	0.04
F-26	0.007856	quasi-spherical	3.44	0.12	0.420	0.013	10.6	0.2	5.37	0.07	1.74	0.04	2.64	0.06
F-27	0.010257	oblong	3.07	0.12	0.66	0.02	11.5	0.3	4.87	0.13	1.65	0.04	3.00	0.08
F-28	0.011988	oblong	3.13	0.07	0.51	0.02	11.2	0.3	4.64	0.11	1.08	0.03	3.00	0.10

Table 1. Fallout glass major element composition, determined by quadrupole ICP-MS. NM, not measured; uncert., expanded uncertainty (coverage factor k = 2).

Sample ID	Na <sub>2</sub> O	MgO	Al <sub>2</sub> O <sub>3</sub>	K <sub>2</sub> O	CaO	FeO
<i>aerodynamic glasses</i>						
F-7	0.98	1.87	1.08	0.96	1.19	1.39
F-8	0.83	1.91	1.17	0.87	1.14	1.42
F-9	0.92	1.93	1.09	0.93	1.33	1.42
F-10	0.97	1.68	1.10	0.96	0.94	1.41
F-11	0.91	1.90	1.09	0.93	1.21	1.38
F-12	0.97	1.73	1.02	0.94	2.00	1.29
F-13	0.92	1.66	1.02	0.90	1.56	1.32
F-14	0.88	1.58	1.04	0.89	1.31	1.31
F-15	0.86	1.99	1.09	0.97	1.06	1.40
F-16	0.95	1.56	1.08	1.00	0.68	1.47
F-17	0.87	1.84	1.12	0.90	1.31	1.37
F-18	0.99	2.00	1.08	0.97	1.18	1.43
F-19	0.95	1.87	1.08	1.10	1.22	1.39
F-20	0.98	1.57	1.06	1.02	0.85	1.40
F-21	0.86	1.52	1.07	1.10	0.79	1.34
F-22	0.94	1.74	1.06	1.16	1.06	1.27
F-23	0.88	1.87	1.16	1.16	1.16	1.35
F-24	0.88	2.01	1.12	1.21	0.99	1.35
F-25	0.93	1.64	1.08	1.06	0.97	1.32
F-26	0.96	1.30	1.02	1.19	1.20	1.20
F-27	0.86	2.03	1.11	1.08	1.14	1.37
F-28	0.87	1.59	1.08	1.03	0.74	1.37

Table 2. Ratios of major element compositions of fallout glass samples relative to the average composition of six sediment samples collected near ground zero.

Sample ID	U ( $\mu\text{g} / \text{g}$ )	uncert.	$^{235}\text{U} / ^{238}\text{U}$ (atom ratio)	uncert.	$^{234}\text{U} / ^{238}\text{U}$ (atom ratio)	uncert.	$^{236}\text{U} / ^{238}\text{U}$ (atom ratio)	uncert.	Th ( $\mu\text{g} / \text{g}$ )	uncert.	$^{230}\text{Th} / ^{232}\text{Th}$ (atom ratio)	uncert.	Pa ( $\text{pg} / \text{g}$ )	uncert.
<i>fallout glass</i>														
F-1	21.400	0.015	5.561	0.004	0.05997	0.00005	0.02697	0.00002	22.78	0.07	3.880E-06	1.9E-08	2.06	0.07
F-2	18.970	0.013	4.134	0.003	0.04459	0.00004	0.02009	0.00002	26.14	0.08	3.659E-06	1.8E-08	2.19	0.08
F-3	19.182	0.014	5.344	0.004	0.05764	0.00005	0.02599	0.00002	18.87	0.06	3.843E-06	1.9E-08	1.82	0.06
F-4	22.102	0.016	5.839	0.004	0.06302	0.00005	0.02838	0.00002	24.78	0.07	3.698E-06	1.8E-08	2.25	0.04
F-5	21.940	0.016	5.057	0.004	0.05456	0.00004	0.02455	0.00002	23.36	0.07	3.805E-06	1.9E-08	2.12	0.05
F-6	25.171	0.018	4.828	0.004	0.05210	0.00004	0.02352	0.00002	23.93	0.07	4.29E-06	2E-08	2.45	0.05
F-7	25.64	0.04	5.461	0.006	0.0592	0.0004	0.0267	0.0003	23.15	0.06	4.278E-06	1.7E-08	NM	-
F-8	31.59	0.06	7.189	0.010	0.0779	0.0006	0.0355	0.0004	25.11	0.07	4.505E-06	1.8E-08	NM	-
F-9	21.16	0.04	4.907	0.007	0.0532	0.0004	0.0240	0.0002	23.31	0.06	3.989E-06	1.6E-08	NM	-
F-10	30.81	0.05	7.093	0.010	0.0770	0.0006	0.0350	0.0004	22.22	0.06	4.692E-06	1.8E-08	NM	-
F-11	24.68	0.04	5.724	0.007	0.0623	0.0005	0.0280	0.0003	23.54	0.06	4.263E-06	1.8E-08	NM	-
F-12	14.73	0.02	2.321	0.003	0.0253	0.0002	0.01161	0.00012	21.09	0.05	4.58E-06	2E-08	NM	-
F-13	22.01	0.04	4.998	0.007	0.0544	0.0004	0.0246	0.0003	23.30	0.06	3.898E-06	1.6E-08	NM	-
F-14	17.41	0.03	4.067	0.005	0.0443	0.0003	0.0200	0.0002	22.76	0.06	3.773E-06	1.8E-08	NM	-
F-15	28.00	0.05	6.418	0.008	0.0700	0.0005	0.0316	0.0003	23.74	0.06	4.78E-06	2E-08	NM	-
F-16	23.98	0.04	6.698	0.009	0.0732	0.0005	0.0330	0.0003	23.23	0.06	4.65E-06	3E-08	NM	-
F-17	26.47	0.05	6.035	0.007	0.0658	0.0005	0.0298	0.0003	24.08	0.06	4.283E-06	1.8E-08	NM	-
F-18	31.96	0.06	6.808	0.009	0.0741	0.0006	0.0334	0.0003	22.54	0.06	4.77E-06	2E-08	NM	-
F-19	16.35	0.03	3.439	0.004	0.0371	0.0002	0.01671	0.00010	23.31	0.06	4.33E-06	3E-08	NM	-
F-20	22.86	0.04	6.214	0.007	0.0670	0.0003	0.0303	0.0002	22.42	0.06	4.32E-06	2E-08	NM	-
F-21	20.19	0.03	5.950	0.006	0.0641	0.0003	0.0289	0.0002	26.80	0.07	3.82E-06	2E-08	NM	-
F-22	22.70	0.04	5.010	0.005	0.0540	0.0003	0.0243	0.0002	24.14	0.06	4.163E-06	1.8E-08	NM	-
F-23	31.45	0.05	7.369	0.008	0.0794	0.0004	0.0360	0.0002	26.17	0.07	4.89E-06	2E-08	NM	-
F-24	25.39	0.04	7.053	0.007	0.0760	0.0004	0.0341	0.0002	22.64	0.06	4.82E-06	3E-08	NM	-
F-25	32.85	0.06	7.725	0.008	0.0833	0.0004	0.0379	0.0002	24.02	0.06	4.62E-06	2E-08	NM	-
F-26	16.17	0.03	4.320	0.004	0.0466	0.0002	0.02108	0.00013	24.25	0.06	3.82E-06	2E-08	NM	-
F-27	23.55	0.04	5.165	0.005	0.0557	0.0003	0.0250	0.0002	23.36	0.06	4.44E-06	2E-08	NM	-
F-28	22.90	0.04	6.619	0.007	0.0714	0.0003	0.0321	0.0002	22.82	0.06	4.27E-06	2E-08	NM	-
<i>sediments</i>														
Sediment-1	2.863	0.004	0.01652	0.00002	0.0001477	0.0000007	0.0000450	0.0000003	24.83	0.07	1.848E-06	1.0E-08	0.939	0.017
Sediment-2	2.708	0.004	0.007321	0.000009	0.0000591	0.0000003	ND	-	21.77	0.06	1.892E-06	1.3E-08	0.800	0.012
Sediment-3	2.980	0.005	0.007302	0.000009	0.0000621	0.0000003	ND	-	21.68	0.06	2.052E-06	1.3E-08	NM	-
Sediment-4	4.327	0.007	0.007246	0.000008	0.0000552	0.0000002	ND	-	21.38	0.07	3.435E-06	1.7E-08	NM	-
Sediment-5	3.805	0.006	0.007250	0.000008	0.0000518	0.0000002	ND	-	23.73	0.08	3.094E-06	1.5E-08	NM	-
Sediment-6	4.578	0.007	0.007251	0.000008	0.0000510	0.0000002	ND	-	21.09	0.07	3.482E-06	1.5E-08	NM	-

Table 3. Actinide concentration and isotopic composition of fallout glasses and sediments, determined by MC-ICPMS. NM, not measured; ND, not detected ( $^{236}\text{U}$  below MC-ICPMS detection limit); uncert., expanded uncertainty (coverage factor  $k = 2$ ).

Sample ID	$^{234}\text{U}$ - $^{230}\text{Th}$ model age (years before 2012)	CSU (k = 2)	$^{235}\text{U}$ - $^{231}\text{Pa}$ model age (years before 2012)	CSU (k = 2)
F-1	165.2	1.3	120	8
F-2	212.6	1.8	151	10
F-3	152.5	1.3	119	8
F-4	163.9	1.3	125	5
F-5	163.8	1.4	122	5
F-6	166.2	1.5	124	5
F-7	153	3	NM	-
F-8	137	2	NM	-
F-9	178	3	NM	-
F-10	129	2	NM	-
F-11	160	3	NM	-
F-12	314	6	NM	-
F-13	166	3	NM	-
F-14	205	4	NM	-
F-15	156	3	NM	-
F-16	172	3	NM	-
F-17	152	3	NM	-
F-18	129	2	NM	-
F-19	269	5	NM	-
F-20	166	3	NM	-
F-21	200	3	NM	-
F-22	179	3	NM	-
F-23	156	2	NM	-
F-24	166	3	NM	-
F-25	129	2	NM	-
F-26	238	4	NM	-
F-27	178	3	NM	-
F-28	165	2	NM	-

Table 4. Calculated  $^{234}\text{U}$ - $^{230}\text{Th}$  and  $^{235}\text{U}$ - $^{231}\text{Pa}$  model ages of fallout glasses. See text for details regarding these calculations. NM, not measured; CSU, combined standard uncertainty (coverage factor k = 2).

Sample ID	atoms <sup>234</sup> U		atoms <sup>230</sup> Th		atoms <sup>232</sup> Th		Number of <sup>230</sup> Th atoms produced by <sup>234</sup> U decay		Number of <sup>230</sup> Th atoms initially present		Decay-corrected <sup>230</sup> Th/ <sup>232</sup> Th	
	/ g sample	st. uncert.	/ g sample	st. uncert.	/ g sample	st. uncert.	49 years before 2012	67 years before 2012	49 years before 2012	67 years before 2012	49 years before 2012	67 years before 2012
F-1	4.92E+14	3E+11	2.29E+11	9E+08	5.913E+16	1.7E+14	6.8E+10	9.3E+10	1.6E+11	1.4E+11	2.7E-06	2.3E-06
F-2	4.13E+14	3E+11	2.482E+11	1.0E+09	6.78E+16	2E+14	5.7E+10	7.8E+10	1.9E+11	1.7E+11	2.8E-06	2.5E-06
F-3	4.37E+14	3E+11	1.88E+11	8E+08	4.896E+16	1.4E+14	6.0E+10	8.3E+10	1.3E+11	1.1E+11	2.6E-06	2.2E-06
F-4	5.13E+14	4E+11	2.38E+11	9E+08	6.430E+16	1.9E+14	7.1E+10	9.7E+10	1.7E+11	1.4E+11	2.6E-06	2.2E-06
F-5	4.99E+14	4E+11	2.308E+11	9.5E+08	6.064E+16	1.8E+14	6.9E+10	9.4E+10	1.6E+11	1.4E+11	2.7E-06	2.2E-06
F-6	5.68E+14	4E+11	2.665E+11	1.2E+09	6.210E+16	1.8E+14	7.9E+10	1.1E+11	1.9E+11	1.6E+11	3.0E-06	2.6E-06
F-7	5.93E+14	4E+12	2.567E+11	1.2E+09	6.009E+16	1.5E+14	8.2E+10	1.1E+11	1.7E+11	1.4E+11	2.9E-06	2.4E-06
F-8	7.59E+14	6E+12	2.935E+11	1.4E+09	6.517E+16	1.7E+14	1.1E+11	1.4E+11	1.9E+11	1.5E+11	2.9E-06	2.3E-06
F-9	4.81E+14	4E+12	2.414E+11	1.1E+09	6.050E+16	1.6E+14	6.7E+10	9.1E+10	1.7E+11	1.5E+11	2.9E-06	2.5E-06
F-10	7.40E+14	6E+12	2.705E+11	1.2E+09	5.766E+16	1.5E+14	1.0E+11	1.4E+11	1.7E+11	1.3E+11	2.9E-06	2.3E-06
F-11	5.77E+14	4E+12	2.605E+11	1.3E+09	6.110E+16	1.6E+14	8.0E+10	1.1E+11	1.8E+11	1.5E+11	3.0E-06	2.5E-06
F-12	2.83E+14	2E+12	2.511E+11	1.2E+09	5.474E+16	1.4E+14	3.9E+10	5.4E+10	2.1E+11	2.0E+11	3.9E-06	3.6E-06
F-13	5.04E+14	4E+12	2.356E+11	1.1E+09	6.046E+16	1.6E+14	7.0E+10	9.5E+10	1.7E+11	1.4E+11	2.7E-06	2.3E-06
F-14	3.84E+14	3E+12	2.229E+11	1.2E+09	5.907E+16	1.5E+14	5.3E+10	7.3E+10	1.7E+11	1.5E+11	2.9E-06	2.5E-06
F-15	6.67E+14	5E+12	2.946E+11	1.5E+09	6.161E+16	1.6E+14	9.2E+10	1.3E+11	2.0E+11	1.7E+11	3.3E-06	2.7E-06
F-16	5.75E+14	4E+12	2.803E+11	1.7E+09	6.029E+16	1.6E+14	8.0E+10	1.1E+11	2.0E+11	1.7E+11	3.3E-06	2.8E-06
F-17	6.25E+14	5E+12	2.677E+11	1.3E+09	6.250E+16	1.6E+14	8.7E+10	1.2E+11	1.8E+11	1.5E+11	2.9E-06	2.4E-06
F-18	7.66E+14	6E+12	2.787E+11	1.4E+09	5.849E+16	1.5E+14	1.1E+11	1.4E+11	1.7E+11	1.3E+11	3.0E-06	2.3E-06
F-19	3.45E+14	2E+12	2.62E+11	2E+09	6.049E+16	1.6E+14	4.8E+10	6.5E+10	2.1E+11	2.0E+11	3.5E-06	3.2E-06
F-20	5.36E+14	3E+12	2.516E+11	1.5E+09	5.818E+16	1.5E+14	7.4E+10	1.0E+11	1.8E+11	1.5E+11	3.0E-06	2.6E-06
F-21	4.70E+14	3E+12	2.651E+11	1.5E+09	6.956E+16	1.8E+14	6.5E+10	8.9E+10	2.0E+11	1.8E+11	2.9E-06	2.5E-06
F-22	5.15E+14	3E+12	2.607E+11	1.3E+09	6.264E+16	1.6E+14	7.1E+10	9.7E+10	1.9E+11	1.6E+11	3.0E-06	2.6E-06
F-23	7.53E+14	4E+12	3.321E+11	1.7E+09	6.793E+16	1.8E+14	1.0E+11	1.4E+11	2.3E+11	1.9E+11	3.4E-06	2.8E-06
F-24	6.05E+14	3E+12	2.831E+11	1.8E+09	5.875E+16	1.5E+14	8.4E+10	1.1E+11	2.0E+11	1.7E+11	3.4E-06	2.9E-06
F-25	7.91E+14	4E+12	2.881E+11	1.6E+09	6.233E+16	1.6E+14	1.1E+11	1.5E+11	1.8E+11	1.4E+11	2.9E-06	2.2E-06
F-26	3.58E+14	2E+12	2.406E+11	1.7E+09	6.292E+16	1.7E+14	5.0E+10	6.8E+10	1.9E+11	1.7E+11	3.0E-06	2.7E-06
F-27	5.37E+14	3E+12	2.693E+11	1.5E+09	6.062E+16	1.6E+14	7.4E+10	1.0E+11	1.9E+11	1.7E+11	3.2E-06	2.8E-06
F-28	5.41E+14	3E+12	2.530E+11	1.3E+09	5.921E+16	1.5E+14	7.5E+10	1.0E+11	1.8E+11	1.5E+11	3.0E-06	2.5E-06

Table 5. Thorium isotope ratios of fallout glasses, corrected for ingrowth of <sup>230</sup>Th by decay of <sup>234</sup>U incorporated in the silicate melt during fallout formation. See text for details regarding this calculation. Ratios are calculated for fallout formed 49 years before 2012 and 67 years before 2012, which are the minimum and maximum possible ages of fallout.